Draft version May 18, 2016
Preprint typeset using LaTeX style emulateapj v. 5/2/11

arXiv:1605.05183v1 [astro-ph.GA] 17 May 2016

THE RED AND FEATURELESS OUTER DISKS OF NEARBY SPIRAL GALAXIES

Aaron E. Watkins[1], J. Christopher Mihos[1], Paul Harding[1]

Draft version May 18, 2016

ABSTRACT

We present results from deep, wide-field surface photometry of three nearby (D=4–7 Mpc) spiral galaxies: M94 (NGC 4736), M64 (NGC 4826), and M106 (NGC 4258). Our imaging reaches limiting surface brightnesses of $\mu_B\sim$ 28 – 30 mag arcsec^{-2} and probes colors down to $\mu_B\sim$ 27.5 mag arcsec^{-2}. We compare our broadband optical data to available ultraviolet and high column-density H I data to better constrain the star forming history and stellar populations of the outermost parts of each galaxy's disk. Each galaxy has a well-defined radius beyond which little star formation occurs and the disk light appears both azimuthally smooth and red in color, suggestive of old, well-mixed stellar populations. Given the lack of ongoing star formation or blue stellar populations in these galaxies' outer disks, the most likely mechanisms for their formation are dynamical processes such as disk heating or radial migration, rather than inside-out growth of the disks. This is also implied by the similarity in outer disk properties despite each galaxy showing distinct levels of environmental influence, from a purely isolated galaxy (M94) to one experiencing weak tidal perturbations from its satellite galaxies (M106) to a galaxy recovering from a recent merger (M64), suggesting that a variety of evolutionary histories can yield similar outer disk structure. While this suggests a common secular mechanism for outer disk formation, the large extent of these smooth, red stellar populations—which reach several disk scalelengths beyond the galaxies' spiral structure—may challenge models of radial migration given the lack of any non-axisymmetric forcing at such large radii.

Subject headings: galaxies:individual(M94,M64,M106), galaxies:evolution, galaxies:spiral

1. INTRODUCTION

Disk galaxies present some of the cleanest laboratories to test theories of galaxy formation and evolution. At first glance, their stellar populations appear distinctly segregated, both spatially and kinematically, with the older, kinematically hotter stars forming central bulges or bars, and the younger, kinematically colder stars forming disks around these bulges. In the hierarchical accretion model of galaxy formation (e.g. Searle & Zinn 1978; White & Frenk 1991; Springel et al. 2005; Vogelsberger et al. 2014), this structure is explained by an "inside-out" formation mechanism, leading to the prediction that the mean age of the stellar populations will be lowest in the disk outskirts. Stars near the galaxy center, formed from primordial gas early in the universe's history, would quickly enrich their local ISM (McClure 1969; Wyse & Gilmore 1992), while in the outskirts the lower gas densities and star formation rates result in reduced enrichment efficiencies (Schmidt 1959; Kennicutt 1998; Bigiel et al. 2008; Krumholz et al. 2012). Thus, there should exist separate, well-defined age-metallicity relationships (AMRs) at individual radii throughout the disk, with an overall negative radial metallicity gradient for stellar populations of a given age (Twarog 1980; Chiappini et al. 1997; Naab & Ostriker 2006). Beyond a certain radius (when the gas density falls below a "critical" value; Kennicutt 1989), one would expect to find very few, if any, stars formed *in-situ*.

This simple and elegant picture, however, is not fully supported by observation. Measurements of the AMR in the solar neighborhood, for example, have shown a much larger dispersion than is expected under such a model (Edvardsson et al. 1993; Haywood 2006). The Milky Way's metallicity gradient also appears to flatten beyond ~ 10kpc (e.g. Twarog et al. 1997; Yong et al. 2005; Maciel & Costa 2010, but see Luck & Lambert 2011, Lemasle et al. 2013); other disk galaxies seem to show similar behavior (e.g. Bresolin et al. 2009; Vlajić et al. 2009, 2011; Sánchez et al. 2014). Also, while many disks show negative age gradients in their stellar populations (e.g. Sánchez et al. 2014), this trend may often reverse beyond a certain radius (e.g. Bakos et al. 2008; Zheng et al. 2015). Finally, disk stars are found to inhabit the very extended outer reaches of the host galaxies, sometimes beyond the apparent star formation threshold radius (e.g. Tiede et al. 2004; Davidge 2006, 2007; Azzollini et al. 2008; Bakos et al. 2008; Vlajić et al. 2009; Martín-Navarro et al. 2014; Okamoto et al. 2015; Zheng et al. 2015), including patches of new star formation (e.g. Thilker et al. 2005; Gil de Paz et al. 2005; Thilker et al. 2007; Lemonias et al. 2011; Yıldız et al. 2015). Under the simple model described above, the presence of these stars is mystifying.

Reconciling these inconsistencies with theory has prompted detailed investigation into the inner workings of disk galaxies, and some amount of consensus is beginning to emerge. Radial migration of stars appears to be important, wherein stars move radially throughout the disk via resonances with inner bars or spiral arms, while maintaining their reasonably circular orbits (Sellwood & Binney 2002; Debattista et al. 2006). Numerous simulations have shown that this process can move stars in excess of a kiloparsec from their birthplaces (Sellwood & Binney 2002; Roškar et al. 2008; Schönrich & Binney 2009; Sánchez-Blázquez et al. 2009; Minchev et al. 2011, 2013), effectively flattening the AMR (Schönrich & Binney 2009; Sánchez-Blázquez et al. 2009; Minchev et al. 2013). Additionally, migration can serve as a means of growing the disk radially even in the presence of a star formation threshold (Roškar et al. 2008; Sánchez-Blázquez et al. 2009; Roškar et al. 2012; Minchev et al. 2012, 2013). While the detailed mechnisms differ in the simulations, a common prediction is

[1] Department of Astronomy, Case Western Reserve University, Cleveland, OH 44106, USA

the creation of a "U-shaped" age gradient in the stellar populations, where older disk stars are found inhabiting both the inner regions of the galaxy and its extended outer disk. Coupled with a flat metallicity gradient in the disk periphery, this would give rise to the "U-shaped" radial color profile observed in most optical bands. In the simulations by Roškar et al. (2008), the break in the age gradient is always coupled to a break in the radial mass and luminosity surface density profiles, and is pushed farther out over time as the stellar disk gains mass (but see Sánchez-Blázquez et al. 2009).

Increasingly, observations appear to support this picture. Bakos et al. (2008), using galaxies in the frequently-observed Stripe 82 of the Sloan Digital Sky Survey (SDSS; York et al. 2000), found that this predicted "U-shaped" color profile is in fact quite common in disk galaxies, and is also commonly coupled to a so-called "Type II" (or downbending: see Pohlen & Trujillo 2006; Erwin et al. 2008) break in surface brightness, in apparent agreement with the simulations of Roškar et al. (2008). However, they found no such break in the mass surface density, in better agreement with Sánchez-Blázquez et al. (2009). Follow-up studies showed similar behavior (Bakos et al. 2008; Gutiérrez et al. 2011; Laine et al. 2014; Martín-Navarro et al. 2014). Studies of outer disks using resolved stars also frequently reveal a shorter scale-length for younger, main sequence populations than for red giant branch (RGB) stars (e.g. Davidge 2006; Vlajić et al. 2009; Radburn-Smith et al. 2011), again implying outer disk populations dominated by old stars, although a break in surface brightness is not always present (as in the case of NGC 300 and NGC 7793; Bland-Hawthorn et al. 2005; Vlajić et al. 2009, 2011).

This schema of radial migration hence appears to be mostly sound, yet exceptions do exist to complicate it. One obvious example is the existence of (again using the nomenclature of Erwin et al. 2008) "Type I" disks (a constant slope exponential surface brightness profile) and "Type III" disks (an upbending break), both of which often show flat color profiles, at a relatively bluer color than the downbending "Type II" disks (Zheng et al. 2015). If the model proposed by Roškar et al. (2008) is universal, such galaxies would require other mechanisms to shape their disks, such as the accretion of low mass satellites (e.g. Younger et al. 2007). However, while Type III disks do show evidence of environmental influences (Laine et al. 2014), the correlation between environment and Type I and Type II disk fractions is unclear (e.g. Pohlen & Trujillo 2006).

Extended ultraviolet (XUV) disks (Thilker et al. 2007) also pose intriguing questions regarding the assumption of a star formation threshold, a seemingly necessary aspect of the models described above. Zaritsky & Christlein (2007) used GALEX imaging to show that that perhaps as many as 50% of disk galaxies contain young (< 400 Myr) star clusters between $1.25R_{25}$ and $2R_{25}$ (out to surface brightnesses of roughly μ_V~29), which, given their number density and assuming a constant star formation history over 10 Gyrs, could fully account for the measured surface brightnesses of starlight at these radii. This would imply that radial migration may not be universally necessary to build outer disks. Indeed, a recent spectroscopic study by Morelli et al. (2015) found mostly negative metallicity gradients in the oldest stellar populations in their sample of disk galaxies, difficult to explain in the context of significant radial migration. Additionally, disk metallicity gradients do not appear to be affected by the presence or absence of bars (Sánchez et al. 2014), in apparent contradiction to the simulations of Minchev et al. (2011, 2012, 2013).

Satellite interactions can also drive evolution in the properties of disks. These interactions can transfer angular momentum to disk stars either directly from the satellite companion (e.g. Walker et al. 1996) or from disk gas driven inwards by the effects of the interaction (e.g. Hernquist & Mihos 1995), leading to a radial spreading of the disk (Younger et al. 2007). Tidal stripping of the satellite companion can also deposit stars in the outer disk of the host as well (e.g. Stewart et al. 2009). Tidal encounters may also induce localized star formation in the disk outskirts (e.g. Whitmore & Schweizer 1995; Weilbacher et al. 2000; Smith et al. 2008; Powell et al. 2013), or potentially generate extremely extended spiral arms (Koribalski & López-Sánchez 2009; Khoperskov & Bertin 2015), which may then form new stars and drive migration of older stars further outwards in the disk. The affects of accretion and tidal interaction, however, depend strongly on the orbital parameters of the encounter (e.g. mass ratios of the interacting galaxies, prograde vs. retrograde orbits, etc.; Toomre & Toomre 1972; Barnes 1988; Quinn et al. 1993; Walker et al. 1996; Bournaud et al. 2005; D'Onghia et al. 2010). This, in combination with progenitors with potentially different structural properties, star formation histories, and metallicity distributions, implies that the influence of accretion and interaction events on disk galaxies ought to be stochastic in nature.

A common thread amongst most of the observational studies cited above, save for those using star counts, is the use of azimuthal averaging when constructing one-dimensional radial profiles of the galaxy light. Such studies measure the surface brightness or color of the disk in successively larger radial bins, thereby maintaining a high signal-to-noise ratio even in the faint outer isophotes of the galaxy. This method has proven extremely useful for large statistical studies (e.g. Pohlen & Trujillo 2006; Erwin et al. 2008; Bakos et al. 2008; Martín-Navarro et al. 2014; Zheng et al. 2015), but it suffers from a number of pitfalls when applied on a galaxy-by-galaxy basis. These techniques "average out" azimuthal asymmetries in the surface brightness and color of the outer disk, which often hold important clues about its dynamical history (see, e.g., the case of M101 Mihos et al. 2013a). These asymmetries may also skew the results of azimuthal averaging by mixing disk light with regions of blank background sky, a particular problem when radial bins with constant ellipticity and position angle are used at all radii (which is often the case; Pohlen & Trujillo 2006; Erwin et al. 2008). In some cases, inferences drawn from azimuthal averaging may even depend on the choice of metric used to construct the profile. For example, in the outskirts of an XUV disk, a luminosity-weighted average surface brightness will present a much different story than an areal-weighted median surface brightness, as most of the light in the outer disk will be contained in just a few blue pockets of star formation (e.g. M83; Thilker et al. 2005). The exact importance of these various pitfalls to azimuthal averaging is not yet clear.

Given these complications, more detailed studies of individual galaxies may provide important new tests for the current paradigm of disk galaxy evolution. For example, if weak spiral arms persist beyond the so-called truncation radius (e.g. Khoperskov & Bertin 2015), this may drive outer disk star formation (Bush et al. 2008) and lead to the radial growth of disks with time; such features may be washed out by an azimuthally-averaged photometric analysis. Bright, nearby disk galaxies provide the best targets for such work; their proximity allows us to study them at high spatial resolution, and also permits follow-up studies of their discrete stellar pop-

ulations. While many spatially resolved studies have been done at high surface brightness ($\mu_B \lesssim 26$) in the past (for just a few examples, see Schweizer 1976; Okamura 1978; Yuan & Grosbol 1981; Kennicutt & Edgar 1986; Tacconi & Young 1990), recent improvements in deep imaging techniques now allow us to probe the outer disks of these galaxies using similar techniques down to the much lower surface brightnesses characteristic of their extreme outer disks.

Here we present deep surface photometry of three large nearby disk galaxies — M106, M94, and M64 — to explore the structure and stellar populations in their outer disks. Taken using the Burrell Schmidt Telescope at Kitt Peak National Observatory (KPNO), our data reach limiting surface brightnesses of $\mu_B \sim$ 28–30 mags arcsec^{-2} in B and V, and we combine our data with extant GALEX and 21cm neutral hydrogen maps of each system to explore the efficacy of different formation mechanisms for outer disks. In Section 2, we present our observation and data reduction strategies; in Section 3, we discuss our methods for extracting and analyzing the surface brightness and color profiles of the galaxies; in Section 4 we present and discuss our results on a galaxy-by-galaxy basis; in Section 5 we discuss the implications of these results in the context of galactic evolution; and in Section 6 we present a summary of our results and conclusions.

2. OBSERVATIONAL DATA

2.1. *Deep Optical Imaging*

We obtained deep broadband imaging of the galaxies M64, M94, and M106 using CWRU's Burrell Schmidt Telescope at KPNO on moonless, photometric nights in Spring 2012 and Spring 2013. Our observing strategy and data reduction techniques are described in detail in (Watkins et al. 2014, and references therein), and we repeat only the most important details here. The telescope's field of view is $1.65^\circ \times 1.65^\circ$, imaged onto a 4096×4096 STA0500A CCD, for a pixel scale of $1.45''$ pixel^{-1}. We observed in two filters: a modified Johnson *B* (2012), and Washington *M* (2013). The latter filter is a proxy for Johnson *V*; it is similar in width but $\sim$ 200Å bluer, and effectively cuts out diffuse airglow from the bright O I λ5577 line (Feldmeier et al. 2002). Each exposure was 1200s in *B* and 900s in *M*, with $\sim$0.5° dithers between exposures to reduce contamination from large-scale artifacts such as scattered light and flat-fielding errors. For each galaxy, the total exposure times are as follows: for M94, 24×1200s (*B*) and 32×900s (*M*); for M64, 23×1200s (*B*) and 30×900s (*M*); for M106, 27×1200s (*B*) and 38×900s (*M*). Sky levels in each exposure were 700 – 900 ADU pixel^{-1} in *B* and 1200 – 1400 ADU pixel^{-1} in *M*.

In addition to the object frames, we also observed offset blank sky pointings for use in constructing night sky flats. We alternated between observing object frames and blank sky frames, in order to maintain similar observing conditions between the two and minimize systematic differences due to changes in telescope flexure and night sky conditions. However, during data reduction we found that the only measurable difference in flat fields constructed from the various subsets of sky frames (taken object by object or run by run) was a mild seasonal gradient that was easily corrected for (for details, see Section 2.2 in Watkins et al. 2014). Thus, in the end we constructed our final sky flat using all sky exposures taken throughout each observing season, resulting in $\sim$100 sky frames in *B* and $\sim$120 in *M*.

Finally, during each season, we also observed Landolt standard fields (Landolt 1992) to derive color terms for each filter, along with deep images of Procyon (1200s in *B*) and Regulus (900s in *M*) to measure the extended point spread function and characterize reflections between the CCD, dewar window, and filter (Slater et al. 2009).

We begin the data reduction by first applying standard overscan and bias subtraction, then correcting for nonlinear chip response and adding a world coordinate system (WCS) to each image. We derive photometric zeropoints for each image using Sloan Digital Sky Survey (SDSS, DR8; Aihara et al. 2011) stars located in the field, converting their *ugriz* magnitudes to Johnson *B* and *V* by adopting the prescription of Lupton (2005) and only using stars within the color range B−V= 0 to 1.5. We use these zeropoints and the color terms derived from the Landolt standard stars to convert our magnitudes into standard Johnson *B* and *V* magnitudes, which we use in all of our analyses throughout this paper. In our final mosaics, we are able to recover converted SDSS magnitudes of SDSS stars in-frame to $\sigma_V = 0.03$ and $\sigma_{B-V} = 0.04$ for all three galaxies. These are hence the *absolute* photometric uncertainties on any magnitudes and colors we quote in this paper; it should be noted that these include the intrinsic scatter in both the transformation between SDSS and Johnson photometric systems, and in the transformation from our custom filters to the Johnson system. However, *relative* photometric uncertainties within a single mosaic are typically much lower than this at high surface brightness ($\sigma_V < 0.01$); at low surface brightness, the relative photometric uncertainty is dominated by uncertainty in the sky-subtracted background. In each mosaic, this background uncertainty (in the vicinity of each galaxy) is typically of order ±1ADU ($\sim$ 0.1% of sky; see above), which implies a global limiting surface brightness of $\mu_{B,lim} \sim 29.5$, although local limiting surface brightnesses vary across each mosaic. The limiting surface brightness in the mosaic of M64 is significantly brighter than the other two ($\mu_{B,lim} \sim 28.0$) due to the presence of foreground Galactic cirrus; we discuss this in more depth in Section 4.2.

We constructed flat fields in each filter using the offset night sky frames. For each sky image, we applied an initial mask using IRAF's[2] *objmask* task, hand-masked any diffuse light missed by *objmask* (typically scattered light from stars located just off frame), and combined the images into a preliminary flat. We then flattened each sky frame using this preliminary flat, modeled and subtracted sky planes from each flattened image, and created a new flat from the sky-subtracted images. We repeated this step five times, at which point the resulting flat-field converged. We then corrected these master flats for the seasonal residual planes described above before applying them to the images.

The last steps of the reduction process consist of star and sky subtraction, followed by final mosaicing. We first subtract the diffuse halos around bright stars following the technique of Slater et al. (2009). These halos arise from both the extended stellar PSF and from reflections between the CCD, dewar window, and filter. We create a model for these halos by measuring them from our deep imaging of Procyon and Regulus, then scale and subtract these models from each star brighter than *V*=10.5 in each frame. We then mask each image of all bright stars and galaxies and fit planes to the diffuse

[2] IRAF is distributed by the National Optical Astronomy Observatory, which is operated by the Association of Universities for Research in Astronomy (AURA), Inc., under cooperative agreement with the National Science Foundation.

night sky background. After subtracting these planes from each image, the images are ready to be combined into the final mosaics. We use IRAF's *wregister* and *imcombine* tasks to create these mosaics, using a median combine after scaling each image to a common photometric zeropoint. Full width half max (FWHM) values of the stellar point spread functions (PSFs) are nearly the same on all mosaics: ∼2.2 pixels, or 3.2″. This large value is a combination of registration error and seeing variations throughout the observing runs; FWHM on individual exposures is typically much smaller (∼1.5″ - 2″).

Once the final mosaics are complete, we also create masked and rebinned versions to improve signal-to-noise at low surface brightness and better reveal faint extended features in the outer regions of each galaxy. The masking process typically only masks pixels brighter than $\mu_B \approx 27$ and $\mu_V \approx 26$, and leaves fainter pixels untouched. After masking, we rebin the mosaic into 9×9 pixel (13″× 13″) blocks and calculate the median in each block to create these "low surface brightness enhanced" mosaics.

2.2. *Ancillary Multi-Wavelength Datasets*

To supplement our broadband imaging, and to study the star forming properties and neutral hydrogen distribution in each of our galaxies, we have obtained ancillary ultraviolet and 21-cm radio data from a variety of sources.

The ultraviolet data comes from several different surveys done by the Galaxy Evolution Explorer (GALEX; Martin et al. 2005) mission, downloaded from the GR6/GR7 data release[3]. The far ultraviolet (FUV; 1350-1750 Å) emission traces recent (< 50 Myr) star formation, while near ultraviolet (NUV; 1750-2750 Å) emission traces slightly older (< 100 Myr) populations, along with some contribution from evolved horizontal branch populations. We use the deepest available images for each galaxy, which come from different surveys; for M94, we used the Nearby Galaxies Survey (NGS; Bianchi et al. 2003); for M64, we used the Calibration Imaging Survey (CIS), in which it appears serendipitously at the edge of the field containing the white dwarf WDST_GD_153_0003 (as such, the M64 UV data is the shallowest); for M106, we used the Deep Imaging Survey (DIS).

Additionally, we obtained H I data from The H I Nearby Galaxies Survey (THINGS; Walter et al. 2008) for M94 and M64, and from the Westerbork H I Survey of Irregular and SPiral Galaxies (WHISP; van der Hulst et al. 2001), for M106. We note that both surveys are interferometric, and hence trace only the relatively high ($> 10^{19}$ cm^{-2}) column density H I. Extended diffuse H I in the outskirts of these galaxies — where we are most interested — may be systematically missed in such surveys.

3. ANALYSIS TECHNIQUES

Our goal is to measure the spatially-resolved properties of each galaxy without the need for complete azimuthal averaging. This allows us to study whether the disk outskirts are azimuthally mixed (as might arise from radial migration scenarios) or show significant azimuthal variations (as might occur if outer disks are shaped by recent accretion events or stochastic star formation). Given the large angular size of our galaxies, as well as the low pixel-to-pixel noise in our final mosaic images, we achieve high photometric accuracy ($\sigma_{B-V} \sim 0.1$ mag at $\mu_B = 27.5$) over scales of ~ 1 kpc. In analyzing each galaxy, we construct azimuthally distinct radial surface brightness and color profiles, and decompose the azimuthal surface brightness variations of the disks into their low order Fourier modes. We give details on each method here. All surface brightnesses are calculated using "asinh magnitudes" (Lupton et al. 1999), which are equivalent to regular magnitudes at high flux levels, but better behaved at low signal-to-noise.

[3] http://galex.stsci.edu/GR6/

3.1. *Surface brightness and color profiles*

For each galaxy, we measure the radial surface brightness and color profiles along six equal-angle radial wedges in the disk plane, increasing the radial width of each bin with radius in order to preserve high S/N in the faint outer regions. By necessity, we use a constant position angle and ellipticity at each radial bin for these profiles; the galaxies often show significant variation in isophotal position angle and ellipticity, and interpretation of the profiles becomes extremely confused if the isophotal bins are allowed to wander. Still, care must be taken in interpreting each profile, particularly in the disk outskirts where background can begin to mix with starlight in portions of each wedge due to misalignment of the aperture with the true, frequently asymmetric isophotes.

We also measure the azimuthally-averaged surface brightness and color profiles for comparison. In this case, we do allow the isophotes to wander, which typically has minimal effect on the qualitative profile shape. However, this choice is occasionally non-negligible; for M106, we found that the surface brightness profiles in both the *B* and *V* bands show clear Type II (downbending) breaks at 550″ when using varying isophotal parameters, but that this break disappears completely when using fixed isophotal parameters. Choice of method thus changes the classification of M106's exponential profile from Type II to Type I. In M94 and M64, profile breaks appear using either method, but the changes in slope are much less abrupt in each case when using fixed parameters over varying parameters. Using varying parameters for the azimuthally averaged profile, but fixed parameters for the angular profiles, also causes the azimuthally-averaged values not to follow the average of all six profiles. In M64, for example, the azimuthally averaged profile favors the major axis due to changing ellipticity in the outer isophotes (a property we discuss in more detail in Section 4.2).

In calculating the profiles, we use the median surface brightness of the pixels in each bin, as it is more robust against contamination from foreground stars or background galaxies. Comparing these profiles to those derived from the total flux in each radial bin shows significant differences in the inner regions, where spiral arms and H II regions dominate the light. In the outskirts, however, the median and luminosity-weighted profiles of the outer regions of each galaxy are nearly identical, due to our masking of bright sources in the disk outskirts. While this masking risks excluding light from bright star forming knots in the disk outskirts, without high-resolution imaging it is often impossible to differentiate between background galaxies, foreground stars, and compact sources within the galaxy itself, and at such faint levels even one such stray source can dominate the total luminosity of a given annulus or wedge. This is a known limitation of deep surface photometry (see, for example, Bland-Hawthorn et al. 2005), and thus to avoid ambiguity with the background, we choose to measure the properties only of the diffuse starlight in the outer regions. To mollify the effects of masking, we

compared our images of each galaxy by eye with GALEX FUV and NUV images to seek out, for example, potential extended star forming regions, but found that such objects are rare. Hence, the populations we sample appear to be representative of the outer disk as a whole.

Given that we perform surface photometry in the faint outskirts using our masked and median-binned images, we correct our surface brightness profiles using sky-subtracted background values measured from these binned images rather than the unbinned images. To measure these values, we place ∼50 equal-sized boxes in regions near each galaxy free of obvious contamination from unmasked sources (in M64's case, this leaves few regions where we can accurately sample the sky due the foreground cirrus contamination), and take the median of the median values of all boxes as the local sky. The sky uncertainty is hence the dispersion in the medians, which is quite small (σ_{sky} ∼0.3 ADU). Within each box, typical pixel-to-pixel variance is found to be ∼1 ADU, with very little variation (σ ∼0.1 ADU) from box to box; hence, we subtract the same sky value from all profiles for a given galaxy.

3.2. *Fourier analysis*

In addition to surface brightness and color profiles, we also conduct a Fourier mode analysis of the azimuthal surface brightness profiles of each galaxy, as a function of radius. This analysis is similar to that described by Zaritsky & Rix (1997); Mihos et al. (2013a); Zaritsky et al. (2013) and others to measure lopsidedness in galaxy disks. We decompose the azimuthal surface brightness profiles as a function of radius into Fourier modes:

$$I(\theta) = \sum_m \cos(m\theta + \phi_m)$$

where I is the intensity, m is the Fourier mode, θ is the azimuth angle, and ϕ_m is the position angle of the m^{th} Fourier mode.

We measure both the $m = 1$ and $m = 2$ mode amplitudes in each galaxy, normalized to the $m = 0$ mode (the mean surface brightness in the annulus), as a function of radius, again using annuli with constant position angle and ellipticity. Typically, $m = 1$ modes are indicative of galaxy lopsidedness, while $m = 2$ and higher modes are related to repeating patterns such as bars or spiral arms. As such, a measurement of $m = 1$ power in the outer disk can be an indication of a tidal disturbance that has not had time to settle (but see Zaritsky et al. 2013), while a measurement of $m = 2$ power in the outer disk might indicate extended spiral patterns. However, $m = 2$ modes may also arise from misalignments between the photometric aperture and the true isophotal shape, due to asymmetries such as warps or tidal distortions in the disk. As such, visual inspection is necessary in interpreting this type of modal analysis to avoid drawing false conclusions.

4. INDIVIDUAL GALAXIES

Here we present the results of our broadband imaging and surface photometry of these three galaxies. For reference, we present various global properties of these galaxies in Table 1.

Figure 1 and subsequent figures show a comparison between our broadband imaging, GALEX FUV and NUV imaging, and THINGS and WHISP H I imaging (see Section 2.3). Our broadband imaging is shown in the upper-left of the figures, with the intensity scale rewrapped over three ranges of brightness (μ_B< 24.6, 24.6 <μ_B< 26.5, and μ_B> 26.5) to highlight different regions. We show the unbinned, native resolution images inside of the μ_B= 26.5 isophote, and the 9 × 9 binned images outside of this isophote in order to enhance faint, extended features. In the upper-right of the figures, we show a B−V pixel-to-pixel color map of our broadband data (at native resolution only). The colorbars on the righthand sides give B−V values. UV data from GALEX is shown in the lower-left of the figures (FUV in blue and NUV in yellow), while 21 cm emission is shown in the lower-right.

Table 1
Galaxy Properties

		M 94 NGC 4736	M 64 NGC 4826	M 106 NGC 4258
(1) RA	[J2000]	12:50:53.0	12:56:43.6	12:18:57.5
(2) Dec	[J2000]	+41:07:14	+21:40:59	+47:18:14
(3) Type		(R)SA(r)ab	(R)SA(rs)ab	SAB(s)bc
(4) Distance	[Mpc]	4.2 [a]	4.7 [b]	7.6 [c]
(5) $M_{B_T^0}$		−19.4	−19.5	−20.9
(6) $(B-V)_T^0$		0.72	0.71	0.55
(7) M_{HI}	$[10^8 M_\odot]$	4.00 [d]	5.48 [d]	35.9 [f]
(8) M_{HI}/L_B	$[M_\odot/L_{\odot,B}]$	0.045	0.056	0.101
(9) R_{25}	[arcmin]	5.6	5.0	9.3
(10) R_{25}	[kpc]	6.8	6.8	20.6
(11) W_{50}	[km s^{-1}]	208.5 [d]	304.0 [d]	381 [g]
(12) $SFR_{H\alpha}$	$[M_\odot$ yr$^{-1}]$	0.43 [d]	0.82 [d]	3.82 [e]
(13) Scale	[pc arcsec^{-1}]	20.4	22.8	36.8

Note. — Rows are: Right ascension and declination (1,2), morphological type (3), adopted distance (4), absolute B magnitude (5), B−V color (6), H I mass (7), H I mass per unit blue luminosity (8), μ_B= 25 isophotal radius in arcminutes (9) and kpc (10), H I line width (11), Hα star formation rate (12), and physical scale (13). All values come from the RC3 (de Vaucouleurs et al. 1991), except for: (a) Radburn-Smith et al. (2011), (b) Jacobs et al. (2009), (c) Humphreys et al. (2013), (d) Walter et al. (2008), (e) Kennicutt (1998), (f) van der Hulst et al. (2001), (g) Tully et al. (2009).

We overlay white ellipses of various semi-major axis length on each image, to provide a visual scale for the surface brightness and color profiles shown in Figure 2 and subsequent figures. Each ellipse uses the parameters (ellipticity and position angle) of the last best-fit isophote of the unbinned image, and is labeled in arcseconds. We also plot two red lines to indicate the major and minor axes of these ellipses, labeled 0° and 90°, respectively, with 0° marking the position angle of the major axis.

Figure 2 and subsequent figures show surface brightness and color profiles of the galaxies, plotted as a function of semi-major axis length (shown in arcseconds and kpc). The colored lines in the top-left (B band surface brightness) and bottom-left (B−V color) panels of Figure 2 represent profiles measured along the corresponding colored wedges depicted in the inset schematic (solid lines indicate where the unbinned mosaic was used, and dashed lines indicate where the 9 × 9 binned mosaic was used). We overplot the azimuthally-averaged profiles of each galaxy as well using black squares (unbinned data) and triangles (9 × 9 binned data). Characteristic error bars are also shown in each figure, dominated by the presence of faint, unmasked background sources. Because this is correlated scatter, the error in color is much less than the quadrature sum of errors in surface brightness (see Rudick et al. 2010). We also include the radial FUV and NUV surface brightness (in AB magnitudes, shifted upward by 2 mags arcsec^{-2} to avoid stretching the ordinate axis of each graph) for comparison, measured using the same isophotes as the optical data: FUV is shown in purple and NUV is shown in gold, plotted only to where the FUV surface brightness begins to flatten into a constant background value. All surface brightnesses and colors have been corrected for foreground extinction using the extinction maps of Schlegel et al. (1998)

as recalibrated by Schlafly & Finkbeiner (2011); we use the coefficients measured by Yuan et al. (2013) to derive the extinction in the two GALEX passbands.

Additionally, we show Fourier $m = 1$ and $m = 2$ amplitudes (normalized to the $m = 0$ amplitudes; see Section 3.2) as a function of semi-major axis length in the righthand panels of Figure 2 and subsequent figures. $m = 1$ amplitudes are shown in the upper right, with their corresponding azimuthal angle plotted just below, while $m = 2$ amplitudes and angles are shown in the bottom-right. Angles are measured in the plane of each galaxy; 0° thus marks the major axis at the galaxy's position angle, increasing clockwise (shown by the red lines in Figure 1 and subsequent figures). Blue symbols are measured from the *B* band images, and gold are measured from the *V* band images. Both bands typically show good agreement except in regions of low signal-to-noise.

4.1. *M94 (NGC 4736)*

M94 (NGC 4736) is part of the Canes Venatici I Cloud (Karachentsev 2005), a loose association of galaxies that may be expanding with the Hubble flow (Karachentsev et al. 2003). It is hence fairly isolated: Karachentsev & Kudrya (2014) list its nearest neighbor as IC 3687, a dwarf galaxy located at roughly the same distance as M94 (∼ 4.5 Mpc; Jacobs et al. 2009; Radburn-Smith et al. 2011), but some ∼ 3° (∼ 240 kpc, in projection) away on the sky (see also: Geller & Huchra 1983). The galaxy contains an outer star-forming structure, often referred to as a 'ring', at ∼ 200″ (4 kpc), which is offset in position angle from the bright inner disk. This ring is also visible in H I (e.g. Bosma et al. 1977; Mulder & van Driel 1993), where it appears as a set of irregular spiral arms at high column density (Walter et al. 2008, this is also true of its appearance in the UV, e.g. Trujillo et al. 2009). Despite this unusual morphology, the gas kinematics show a monotonic rotation curve from the center out (Bosma et al. 1977; Mulder & van Driel 1993), however noncircular motions are prevalent throughout the disk at small spatial scales (Walter et al. 2008). There is evidence that these outer spiral arms, as well as a more strongly star-forming inner ring inside of 50″, are the result of Lindblad resonances (Gu et al. 1996, Trujillo et al. 2009; it is also interesting to note that the inner and outer rings both have approximately the same position angle; Mulder & van Driel 1993). Planetary nebulae (PNe) kinematics also show evidence of flaring in the old stellar populations (Herrmann et al. 2009; Herrmann & Ciardullo 2009) that may imply some past perturbation. Overall, the galaxy is difficult to characterize, and shows many asymmetric features indicative of a possible recent interaction, despite its rather isolated neighborhood.

Figure 1 shows these asymmetric features, all located inside of 500″(10 kpc). The outer spiral arms can be traced in our B−V color map, the GALEX images, and in the H I, and show strong north-south asymmetry and several kinks qualitatively similar to those found in the grand-design spiral arms of NGC 5194 (Dobbs et al. 2010), a galaxy known to be interacting with its S0 companion NGC 5195 (Toomre & Toomre 1972; Salo & Laurikainen 2000; Durrell et al. 2003). Beyond this radius, however, both the UV and 21cm emission drop off abruptly, leaving only the smooth optical isophotes. The outer disk profile continues dropping exponentially with no sign of any break out to at at least 20 kpc (∼ 9 outer disk scale lengths). While the azimuthally averaged surface brightness profile of the galaxy shows a mild flattening in the last two points (at μ_B∼ 30), suggestive of transition into a smooth halo, this is in fact well-modeled by a transition from the disk to the local background. We also identify a faint plume visible on the southwest side, the source of an upturn in surface brightness along the southwestern minor axis wedges (yellow and purple curves) shown in Figure 2; while this plume may be part of M94's disk, it is too faint ($\mu_B >$ 29) to constrain its color.

M94's B−V color profile (bottom left in Figure 2) shows a blueward color gradient in the disk between 200″ and 500″ (4 – 10 kpc), at which point the gradient reverses (this behavior can also be seen in the $g - r$ profile shown by Trujillo et al. 2009, though we trace the red part of the profile some 200″ beyond the apparent limit of their data). The FUV and NUV profiles both show a spike in surface brightness at the tail end of the blue gradient, coincident with the outer spiral arms; beyond this point, however, the UV profiles truncate. This same behavior appears in the high column-density H I gas as well, though lower column-density gas may well exist beyond this radius.

The six angular surface brightness and color profiles of the disk show little spread beyond this radius as well. Each color profile turns redward at roughly the same radius, albeit with varying degrees of sharpness. The southwest side of the galaxy shows the mildest gradients; from Figure 1, this is also where the spiral arms appear weakest. Otherwise, the average interquartile spread amongst all six wedges beyond the break in the color profile is only $\Delta\mu_B$ ∼0.2 and Δ(B−V) ∼0.02. As such, it appears that the bulk of the recent star formation in the disk ends with the outer spiral arms; if star formation occurs beyond this radius, it is either at extremely low levels ($\mu_{FUV,AB} < 5 \times 10^{-5} M_\odot$ yr^{-1} kpc^{-2}) or very localized such that we smooth over it in our angular bins as well. However, visual inspection of the FUV image and the B−V colormap shows no obvious patches of new star formation in the outer disk.

Additionally, the $m = 2$ amplitude weakens outside of this radius, lending credence to the idea of an azimuthally smooth outer disk. The strong $m = 2$ mode seen inside of 200″ (4 kpc) is driven by an offset between the inner and outer disk, specifically the gap between the inner disk and the outer spiral arms. We find some evidence of lopsidedness beyond 300″ (6 kpc), though it is mild ($A_1/A_0 \sim 0.2$). In the final radial bin, the $m = 1$ and $m = 2$ amplitudes peak sharply in the *B* band (and to some extent in *V*), however the azimuthal variations in surface brightness in low S/N regions is sensitive to background fluctuations, hence caution is warranted in their interpretation. That said, this final radial bin does encompass the southwestern plume, which may be driving some of the non-axisymmetric power.

Given the smoothness of the outer disk, it is worth discussing the distorted inner disk morphology in more detail. Inside of ∼200″ (4 kpc), the disk is offset significantly in position angle from the outer disk, suggestive of a tilt in inclination between the two. However, due in part to the noticeable offset between the H I kinematical major axis and the optical major axis of the inner disk (Bosma et al. 1977; Kormendy & Norman 1979), M94 has long been thought to host an oval distortion, a type of disk instability similar to a bar but larger in physical scale (a good overview of oval distortions can be found in Section 3.2 of Kormendy & Kennicutt 2004). Early density-wave models suggested that oval distortions may maintain spiral structure (this was proposed, but not explored, by Toomre 1969), acting in a manner very sim-

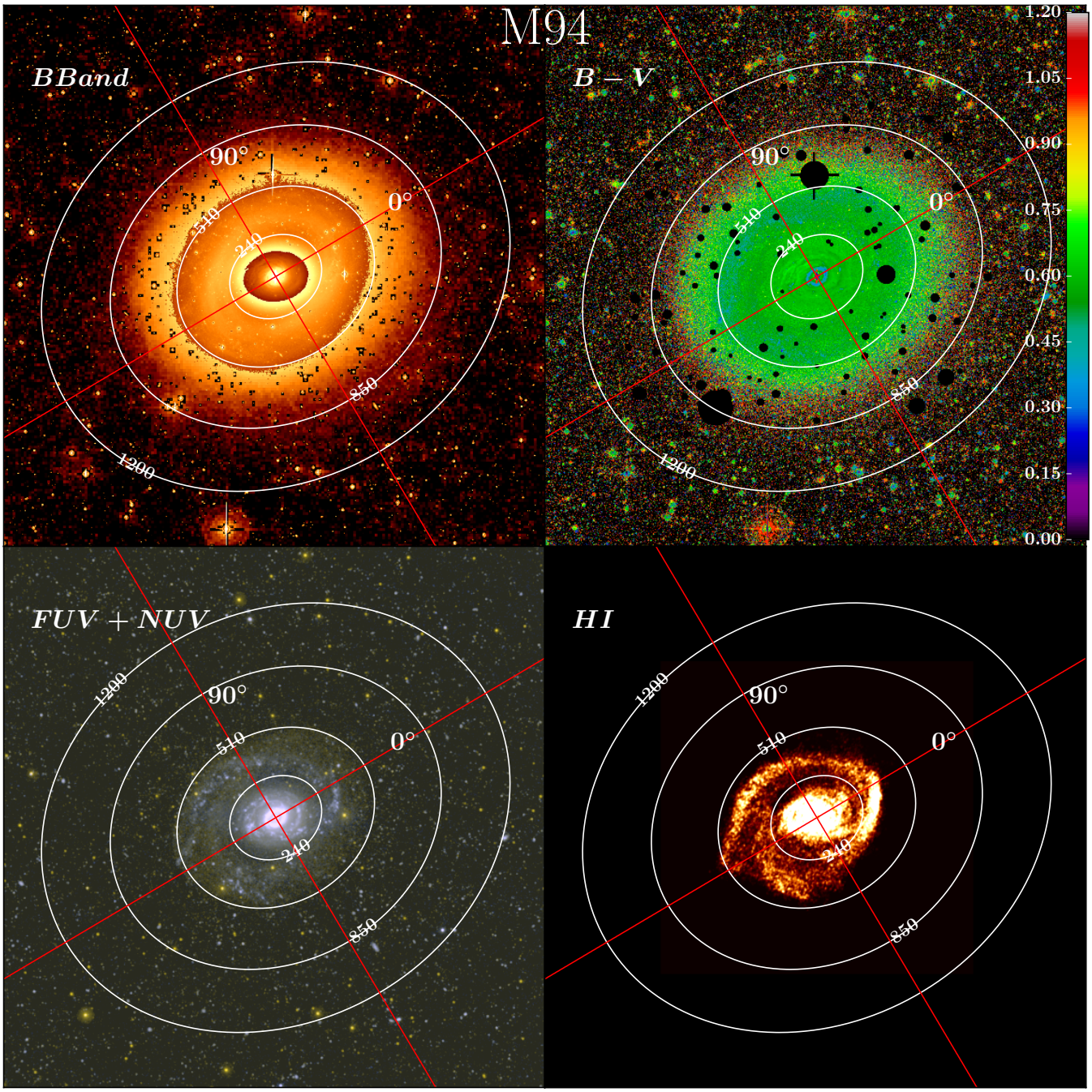

Figure 1. Images of M94, with ellipses of various semi-major axis length overplotted for reference, labeled in arcseconds. Red lines indicate the major and minor axes of the outermost isophote of the unbinned image; labeled angles give degrees from the chosen galaxy position angle for the Fourier analysis discussed in Section 3.2. From the top left: **1.)** A subset of our *B* band mosaic, rescaled in intensity to highlight ranges of surface brightness ($\mu_B <$ 24.6, 24.6 $< \mu_B <$ 26.5, and $\mu_B >$ 26.5); the 9×9 median binned image is shown outside of $\mu_B >$ 26.5 to enhance diffuse features; **2.)** B−V color map; B−V values are shown via the colorbar on the righthand side; **3.)** *FUV* and *NUV* false-color image constructed from GALEX data, specifically the Nearby Galaxy Survey (NGS; Bianchi et al. 2003); blue denotes FUV data, yellow denotes NUV data; **4.)** H I image constructed from THINGS data (Walter et al. 2008); 1σ rms noise of this image is $2.6{\times}10^{20}\mathrm{cm}^{-2}$ (Walter et al. 2008). All four plots are shown at an identical angular scale.

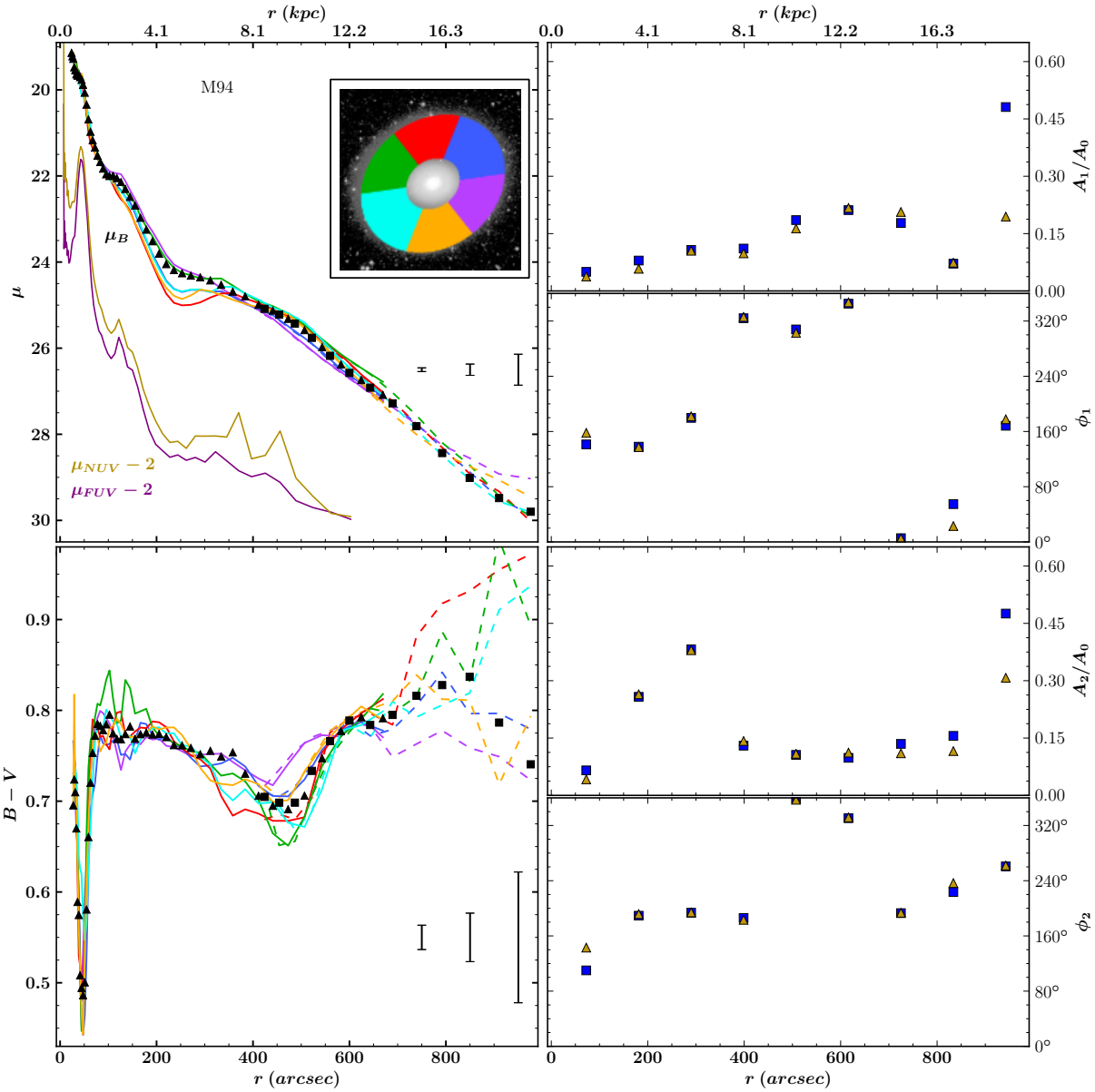

Figure 2. **Top Left:** *B*, *FUV*, and *NUV* surface brightness profiles of M94. Triangles and squares are azimuthally-averaged values, while colored lines are profiles averaged over the corresponding colored wedges shown in the inset schematic. Triangles and solid lines denote where unbinned data is used, and squares and dashed lines denote where the 9 × 9 binned data is used (see Section 2.2). The purple and gold lines show the FUV and NUV profiles, respectively; UV surface brightnesses are shifted brighter by 2 magnitudes to avoid stretching the y-axis, and are cut off just before the FUV surface brightness profile flattened to the background value. All values are corrected for foreground extinction. Representative error bars are shown for μ_B=28, 29, and 30. Error bars are smaller than the point sizes for surface brightnesses below these values. **Bottom Left:** B−V profiles of M94. Symbols and colors used are the same as the top left plot. UV colors are not plotted. Values are also corrected for foreground extinction. Representative error bars are shown for μ_B=26, 27, and 28. **Top Right:** m = 1 amplitude normalized to m = 0 amplitude (top) and angle (bottom) of the azimuthal intensity profile, plotted as a function of semi-major axis length (see Section 3.2). Blue squares indicate values obtained from the *B* band image, and gold triangles indicate values obtained from the *V* band image. **Bottom Right:** m = 2 mode normalized amplitude and angle of azimuthal intensity profiles, as above. We assume a distance of 4.2 Mpc to M94 (Radburn-Smith et al. 2011), for a disk scale length of 2.3 kpc (based on the outer disk).

ilar to bars (Kormendy & Norman 1979; Athanassoula 1980; Kormendy & Kennicutt 2004). In simulations, Trujillo et al. (2009) found that an oval distortion in the inner disk provided a good match to M94's observed structure, lending additional support to the idea.

We examine this idea again using our surface photometry. M94's surface brightness profile is complex; Trujillo et al. (2009) stated that M94 may be considered an antitruncated disk, given the nearly flat profile in the outer spiral arm region (300″ – 400″, 6 – 8 kpc), unless the inner disk was truly an oval distortion, in which case it would be better classified as a single-exponential. In contrast, Herrmann & Ciardullo (2009) used PNe kinematics to explain this flattening as an increased importance of a thick disk component in the outer regions. It is thus interesting to note that the surface brightness profile of the galaxy shows a larger inner disk scale length (0.8 kpc, measured between 85″ and 165″) along the minor axis (green and purple curves in Figure 2) than the major axis (0.6 kpc). This difference becomes most notable around 200″(4 kpc), coincident with the gap between the inner disk and outer spiral arms. Thus, M94's surface brightness profile appears more cleanly exponential when the inner disk-outer-disk gap is avoided.

The smoothness of M94's profile thus provides additional evidence in favor of a continuous stellar disk, favoring the oval distortion model over an outside accretion event to explain the galaxy's structure. This explanation may not contradict the results of Herrmann & Ciardullo (2009); resonances with bars or similar features can drive vertical heating and lead to larger scale heights (Schönrich & Binney 2009, but see Minchev et al. 2012). While the mild lopsidedness of the outer isophotes may be evidence of recent interactions, lopsidedness is extremely common even in isolated galaxies (Zaritsky et al. 2013), and may in fact be a signature of misalignment between the stellar disk and dark matter halo. As such, the idea of M94 as a solitary, isolated galaxy evolving in an almost purely secular way appears sound. M94 may thus serve as a particularly interesting target for future studies investigating the effect of secular processes such as radial migration on outer disks.

4.2. *M64 (NGC 4826)*

M64 (NGC 4826) is a nearby Sa galaxy, alternately referred to as the "Black Eye" or "Evil Eye" galaxy (else the "Sleeping Beauty" galaxy; Rubin 1994) due to the prominent dust lane near the bulge on the northeast side. Interest in the galaxy peaked when Braun et al. (1992) discovered that the inner (< 50″, 1 kpc) and outer (> 50″) H I disks counter-rotated with respect to each other. Subsequent observations by Rix et al. (1995) revealed that the entire stellar disk co-rotates with the inner gas disk, implying that the outer gas disk is an accretion relic. Detailed study of the H I (Rubin 1994) and CO (García-Burillo et al. 2003) showed evidence of shocks and radial inflow in the inner disk originating from the boundary between the two counter-rotating systems. Indeed, simulations reproduce such inflows, as angular momentum cancellation at the boundary between the counter-rotating components leads to gas infall (Quach et al. 2015). The galaxy also shows evidence of both leading and trailing stellar spiral arms (Walterbos et al. 1994), suggestive of some disturbance in the stellar disk as well, but nonetheless the disk shows an extremely regular exponential surface brightness profile out to ∼300″. Despite the galaxy's counter-rotation and overall low H I surface densities, the H I rotation curve is quite regular as well (de Blok et al. 2008; Walter et al. 2008).

We show our imaging of M64 in Figure 3, along with the radial surface brightness, color, and Fourier profiles in Figure 4. Unfortunately, M64 lies in a region of the sky rife with contamination by foreground Galactic dust (or 'cirrus'), which severely limits the depth of our mosaics of this galaxy. Whereas we can probe surface brightnesses of $\mu_B\sim$ 30 in M94 and M106, here we begin transitioning into the background at $\mu_B\sim$ 28.5 due to the surrounding cirrus. Because of the asymmetric nature of the cirrus, we cannot measure the Fourier modes of the disk beyond 600″, where the dust begins to significantly skew the analysis.

Spiral structure is most obviously seen in our B−V colormap, and appears constrained to within roughly 200″(4.5 kpc). The disk color profile is also generally much flatter than M94's. From Figure 4, we see a mild blueward gradient between 100″ and 200″ (∼2 – 4.5 kpc), beyond which the profile flattens out at B−V∼0.75. A single mild (∼0.02 magnitude) blueward dip appears at ∼450″ (9.5 kpc), and the color trends continuously redder beyond this radius. The majority of the UV light is found within the spiral arms; both the FUV and NUV profiles show a steep decline with radius, reaching μ_{NUV} ∼30 by ∼200″ (4.5 kpc). Within this radius, the H I shows weak spiral structure as well, while at larger radius the gas distribution is quite irregular and patchy, with extremely low column density (< 10^{20}cm^{-2}; de Blok et al. 2008). The rapid decline in UV surface brightness and very low outer H I column density both argue that recent star formation in M64 is constrained to the inner 4.5 kpc.

The presence of both leading and trailing spiral arms in this galaxy (Walterbos et al. 1994) implies a disturbed stellar disk as well, and indeed, distorted isophotes are visible just outside of 170″(4 kpc), and, more weakly, just outside of 340″(7 kpc) as a slight protrusion on the galaxy's west side. The angular profiles also show more scatter beyond ∼175″, with mild but significant power in the $m = 1$ and $m = 2$ modes at these radii as well. Close examination of the images shows that most of the $m = 2$ power comes from misalignment of the elliptical aperture with the galaxy isophotes, rather than due to any spiral structure. The slow angular slewing of the $m = 2$ mode thus implies a gradual shift in the outer isophotes' position angle with respect to the photometric aperture. Indeed, from our *ellipse* analysis, we find that the position angle steadily increases by ∼ 20° between 200″ and 700″(4.5 – 15 kpc).

The most notable feature we find in M64, however, is the dramatic antitruncation of the profile beginning around 400″ (9 kpc). We note that the same break is seen in the *R* band profile of (Gutiérrez et al. 2011). The immediate concern is that this feature is induced by the foreground cirrus, however a battery of tests demonstrates that this is not the case. While the cirrus contamination seems severe in the northwest and southeast sides of our optical image, its surface brightness in these regions lies around μ_B= 28.0 to 28.5. As this Type III upbending break begins roughly 2 magnitudes brighter than this level, it cannot be caused simply by a transition to this background. Additionally, the break can be seen along every angular cut at the same radius; this would only be true if the cirrus were evenly distributed around the galaxy, which Figure 3 shows is not true. The effect of the cirrus on the galaxy's surface brightness profile thus appears to be mild; indeed, it seems strongest only at the largest radii, where the northwest profiles (blue and red curves) flatten off most quickly, at the expected background levels ($\mu_B\sim$ 28.0). The eastern major axis profile (cyan) shows the lowest surface brightness, and is

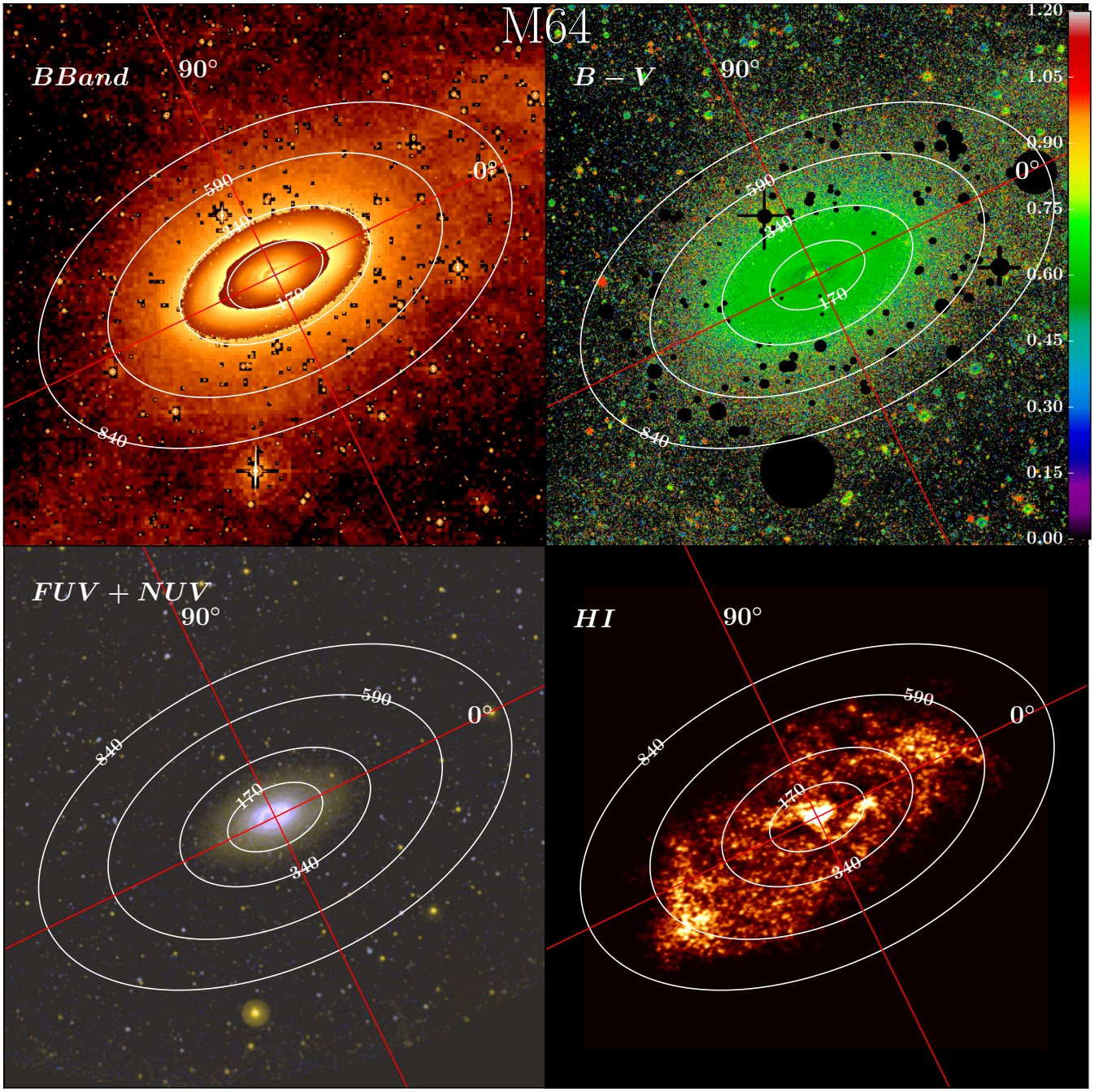

Figure 3. Imaging of M64, using the same layout as Figure 1. GALEX data is from the Calibration Imaging survey (CAI); M64 appears serendipitously near the edge of the field, and exposure times differ between NUV and FUV (~7000s and ~1000s, respectively). 1σ rms noise of the H I image is 3.4×10^{20}cm^{-2} (Walter et al. 2008).

also the wedge with the least cirrus contamination.

This antitruncation thus appears inherent to the galaxy. Inside of the break radius (between 200″ and 400″) the interquartile spread between the six angular profiles is $\Delta\mu_B$ ~0.2 and Δ(B−V) ~0.01, indicating a very uniform stellar population despite the asymmetry in the disk. Beyond the profile break, all the angular profiles trend redward, save for the northern (red) wedge. The reason for the discrepant northern wedge is not evident, even upon close examination of the image. It may be related to the cirrus; we measure a color of B−V~0.7 in the relatively bright patch just to the northwest of M64, which is also the color at which the northern profile flattens out. While showing some patchiness, the mean color of the background near M64 (which includes contributions from cirrus, unresolved background sources, and residual sky variance) is B−V=0.85. Thus, we tested the cirrus' influence on all of the color profiles using a simple model — a screen with a uniform surface brightness of μ_B= 28 and a uniform color of B−V=0.8 overlaid atop a model galaxy with a similar surface brightness and color profile as M64 — and found that it begins to affect M64's color profile at a surface brightness of μ_B~27.0, or a radius of ~450″. As such, it appears that the

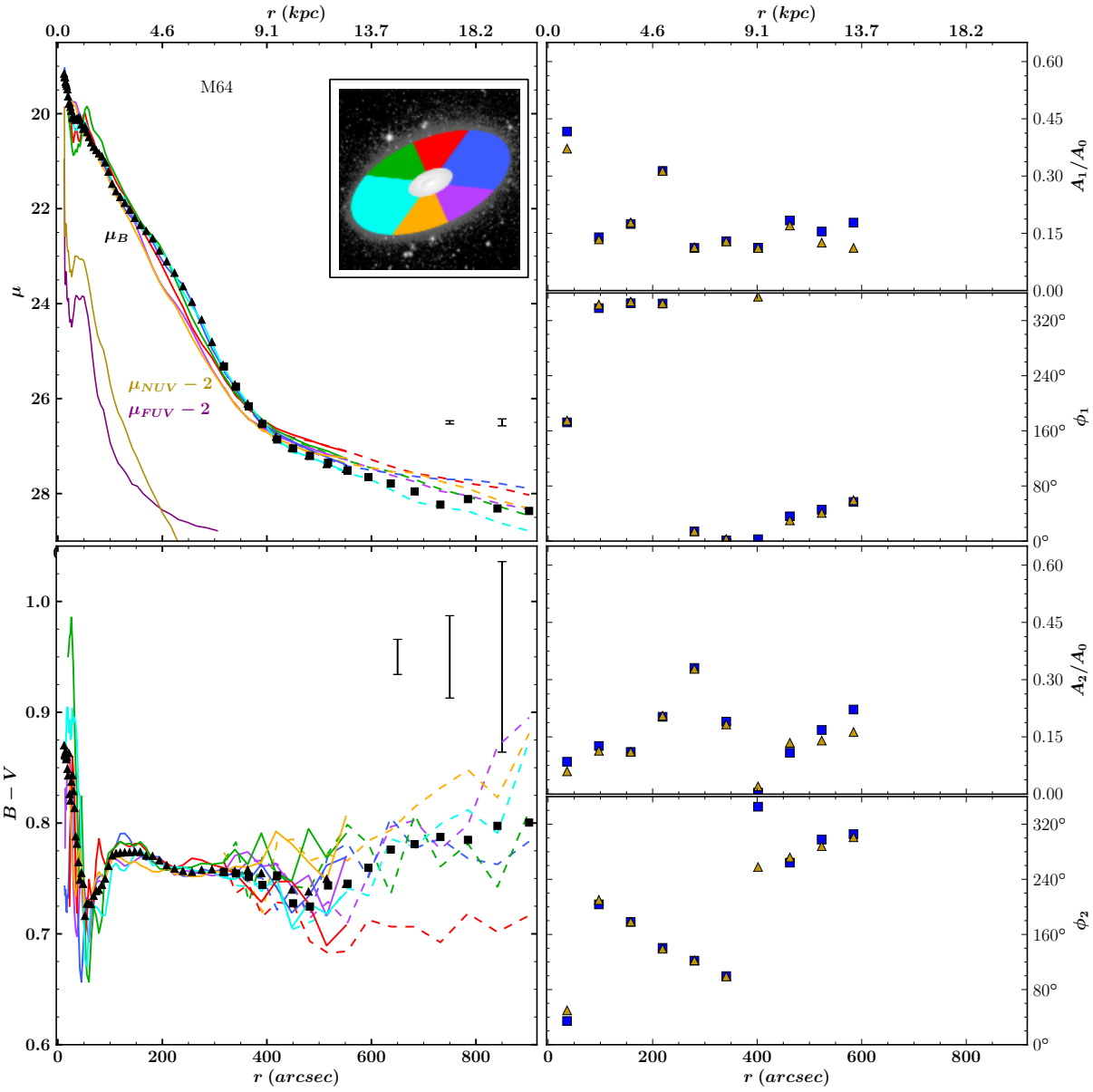

Figure 4. Photometric analysis of M64, using the same layout as Figure 2. The Fourier analysis stops at a smaller radius than the photometric profiles due to contamination from asymmetrically distributed foreground dust (see text). The limiting NUV surface brightness is much lower than the limiting FUV surface brightness due to the difference in exposure times between the two filters. We show representative surface brightness error bars only for μ_B=27 and 28 for this galaxy, as the limiting surface brightness for this galaxy is μ_B~28.5 (see text). We show the same representative color error bars as Figure 2, however. We assume a distance of 4.7 Mpc to M64 (Jacobs et al. 2009), for a disk scale length of 1.4 kpc (based on the inner disk).

redward color gradients beyond ~450″ should be attributed to the foreground cirrus, and not to changes in stellar populations within the galaxy. We thus do not consider the color profile beyond ~450″ for the remainder of our analysis.

If the upbending profile seen in Figure 4 is due to a distinct outer disk, it may have been spawned from the interaction that led to the counter-rotating kinematics seen in M64. If so, its red colors rule out, for M64, models where anti-truncated outer disks are built through induced star formation in extended gas (a mechanism suggested by Laine et al. 2014) and instead favor scenarios where angular momentum exchange during a merger migrates stars into the disk outskirts and forms a Type III break (e.g., Younger et al. 2007). However, the profile presents problems for the latter scenario as well. The models of Younger et al. (2007) display mild breaks (h_{out}/h_{in} = 1.2 – 1.8) which occur at relatively small radius (R_b/h_{in} = 2.5 – 4), while the break we see in M64 happens at much larger radius (R_b/h_{in} = 6) and is significantly

more dramatic (h_{out}/h_{in} = 10). Furthermore, from our *ellipse* analysis, outside of the break M64's outer isophotes become much rounder (b/a = 0.7) than in the inner disk (b/a = 0.5), which wouldn't arise from simple radial spreading of the disk. Taken together, these arguments suggest we are not seeing an outer disk formed through angular momentum transfer during an accretion event, but instead a profile transitioning from a disk component to an outer halo.

This alternative interpretation of upbending profiles was also proposed by Martín-Navarro et al. (2014), who argued that no true Type III disks exist, and that upbending profiles simply signal the presence of a stellar halo. Under the more detailed classification scheme proposed by Pohlen & Trujillo (2006), this would include the Type III-s galaxies (spheroidal): galaxies with a Type III break that show progressively rounder isophotes beyond the break radius. To test this idea further regarding M64, we fit a variety of models to its surface brightness profile using *emcee*, a Python-based Markov Chain Monte Carlo (MCMC) sampling algorithm (Foreman-Mackey et al. 2013). While a double exponential model provides a good fit to the data, we found nearly equally good fits for a disk+power law model with a power law slope of α ~-2, or disk+Sérsic profiles with indexes n ~0.5 and 4. Hence in the end we find that the fits do not provide discrimination amongst the various models. Given this, the rounding of the outer isophotes and the poor match to models of outer disk formation leads us to prefer the disk+halo interpretation for M64's overall profile.

With all the evidence that M64 has suffered a recent merger, do we see signatures in its photometric structure? While the galaxy shows some lopsidedness within r =200″(4.5 kpc; Figure 4), we see no obvious tidal features in the outer disk that might signal a past accretion event, although the foreground cirrus precludes us from probing the faintest levels. While infalling companions can cause significant vertical heating in disks (e.g. Barnes 1988; Toth & Ostriker 1992; Stewart et al. 2008; Kannan et al. 2015), it is less clear how such accretion could have heated M64's disk to form the smooth, diffuse outer spheroid while also depositing a thin H I disk into the rotational plane. This argues that the outer spheroidal component may predate the merger, rather than forming during the event. M64 thus appears to be a case of merger-induced quenching, where the counter-rotating accretion has disrupted the galaxies gaseous disk and shut off the bulk of star formation throughout the system, while leaving the stellar disk largely intact. In this way, we may be witnessing the end stages of M64's transition into an S0 galaxy (e.g. Borlaff et al. 2014).

4.3. *M106 (NGC 4258)*

M106 (NGC 4258) is the brightest member of the Canes Venatici II Group (Fouqué et al. 1992), and can be considered a Milky Way analogue given its similar luminosity, Hubble Type, and local environment (e.g. Kim et al. 2011). While the central regions of M106 have been studied extensively (specifically, to determine the origin of a pair of offset "anomalous" spiral arms; Courtès & Cruvellier 1961; van der Kruit et al. 1972; Pietsch et al. 1994), previous studies on the outer disk are relatively scarce. M106 is the most massive galaxy of the three examined in this paper, and is also the only one of the three with clearly visible satellites. The galaxy NGC 4248, located to the northwest of M106 (labeled in Figure 5), has long been suspected to be a satellite (van Albada 1977), although previous studies found no clear evidence of interaction (e.g. van der Kruit 1979). A Tully-Fisher distance places the galaxy at 7.4 Mpc (Karachentsev et al. 2013), essentially the same distance as M106. The galaxy to the southeast, UGC 7356 (also labeled in Figure 5), is also a companion, of much lower mass (Jacobs et al. 2009; Spencer et al. 2014). The velocity spread between the three galaxies is comparable to M106's rotation velocity, suggesting the companions are bound to M106. Spencer et al. (2014) also finds 7 additional probable satellites of low mass ($-12 > M_V > -17$) within 200 kpc (projected) of M106, indicating a fairly rich local environment.

We present multiwavelength images of M106 in Figure 5, and the photometric profiles in Figure 6. M106 has more prominent UV emission than either M94 or M64, reflecting a higher star formation rate (SFR); indeed, M106's Hα-derived SFR is 3.82 $M_\odot$ yr^{-1} (Kennicutt 1998), compared to 0.43 $M_\odot$ yr^{-1} and 0.82 $M_\odot$ yr^{-1} for M94 and M64, respectively (Walter et al. 2008). A rough estimate using the RC3 colors and the B−V to M/L conversion factors of Bell & de Jong (2001) also implies that M106 has a specific star formation rate roughly a factor of three higher than the other two galaxies. Thilker et al. (2007) classified M106 as a Type 1 XUV disk, defined as a galaxy containing highly structured UV complexes beyond where the UV-derived star formation rate surface density drops below $\Sigma_{SFR} = 3\times10^{-4}$ $M_\odot$ yr^{-1} kpc^{-2}. Again, our B−V colors trace the UV emission well; of note are the extended spiral arms beyond 300″ (10 kpc), and the plume of UV emission and H I on the galaxy's south side (near the companion UGC 7356). This plume, and another on the galaxy's north side (including some of the diffuse UV light inside of 600″), drive the XUV disk classification. Three diffuse patches of UV emission can also be found tracing the extremely faint tail of H I extending from the galaxy's east side (seen crossing the 965″ ellipse in Figure 5), and are also visible as small patches of diffuse light in our optical imaging (we note that these are not visible in Figure 5, as each patch is only a few arcseconds in radius and quite faint).

We see a sharp decline in the UV emission beyond the XUV disk, at roughly 600″ (22 kpc), yet the optical light continues to show an exponential profile well beyond this radius. From Figure 6, the B−V color profile turns sharply redward at this radius as well. As with M94 (and to some extent M64), all angular cuts show the same behavior; the spread amongst the cuts, however, is much greater than in M94 or M64: $\Delta\mu_B$ ~0.5 and Δ(B−V) ~0.07. This is due to irregular isophotes; the minima in the color profiles occur at increasingly large radius from the northeast (red) curve to the west (purple) curve. This trend follows the morphology of the spiral arms, which are stronger on the east side of the galaxy. The northmost (blue) profile breaks the pattern, however it is clear from Figure 5 that the spiral structure is much weaker along this cut. These red disk outskirts extend to at least 40 kpc, some 20 kpc beyond the apparent UV cutoff radius in this XUV galaxy and again appears devoid of strong spiral structure: note the decline in the m = 2 amplitude beyond ~600″ (22 kpc), as seen in Figure 6.

The two bright dwarf companions present one very clear difference between M106 and the other two spirals in our study. Our deep imaging shows clear evidence of tidal distortion in the brighter companion NGC 4248 (Figure 7): its low surface brightness outer isophotes are extremely boxy, and offset in position angle from the dwarf's inner regions by almost 45°. In this aspect, it appears quite similar to NGC

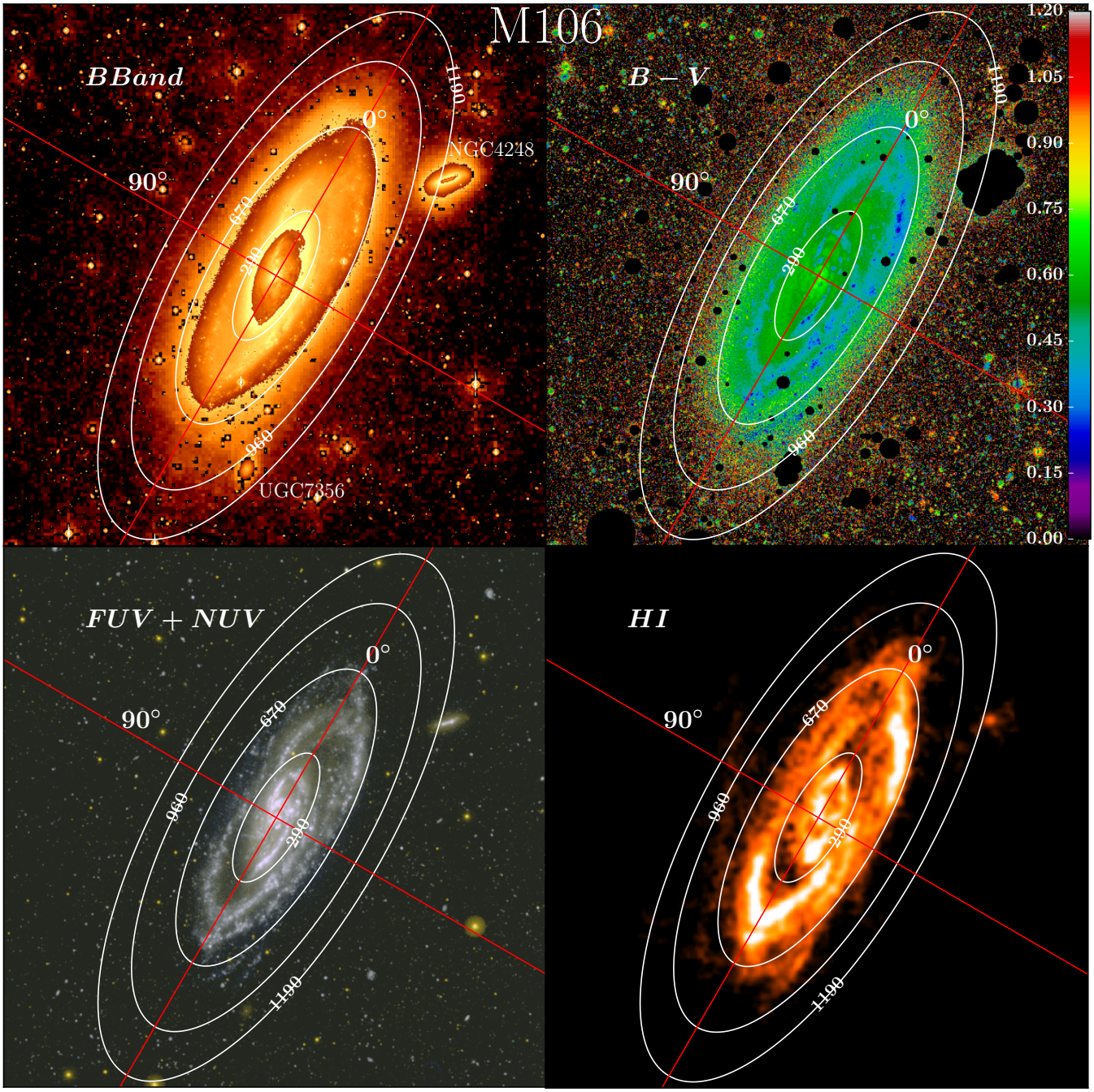

Figure 5. As Figure 1, but of M106. GALEX data is from the Deep Imaging Survey (DIS), and H I data is from the WHISP survey (van der Hulst et al. 2001, 30″ resolution shown); 1σ rms noise is $\sim 10^{20}$cm^{-2}. The companion galaxies NGC 4248 and UGC 7356 are labeled in the *B* band image (upper left).

205, a satellite companion to M31 of comparable luminosity. Like NGC 4248, NGC 205 also shows recent star formation very near its center (Cappellari et al. 1999) along with isophotal twisting (Choi et al. 2002) and a strongly boxy morphology in its outer regions as well (seen in an image taken by S. van den Bergh, presented in Kormendy 1982). A study of RGB star kinematics in NGC 205's outskirts revealed strong high-velocity tails and a reversal in the direction of rotation beyond 1 kpc, indicative of tidal interactions with M31 (Geha et al. 2006). The boxiness in NGC 4248's outer isophotes appears to result from an overlap of an extended elliptical component with symmetric tidal features extending from the north and south sides of the galaxy. Though NGC 4248 is tentatively classified as irregular (de Vaucouleurs et al. 1991), its warped inner isophotes (Figure 7) and rotating H I (van Albada 1977) imply a disklike structure. This galaxy may thus serve as an example of a low mass disk being tidally transformed into a dwarf elliptical more akin to NGC 205, an intriguing idea in the context of M106 as a Milky Way (or M31) analog.

In turn, the effect of the companions on M106's outer disk may be seen in the disk's visible warp, seen both in the H I kinematics (van Eymeren et al. 2011) and in the generally high $m = 1$ amplitude at all radii in this galaxy (Figure 6). The $m = 1$ mode peaks around 600″, near the outer spiral

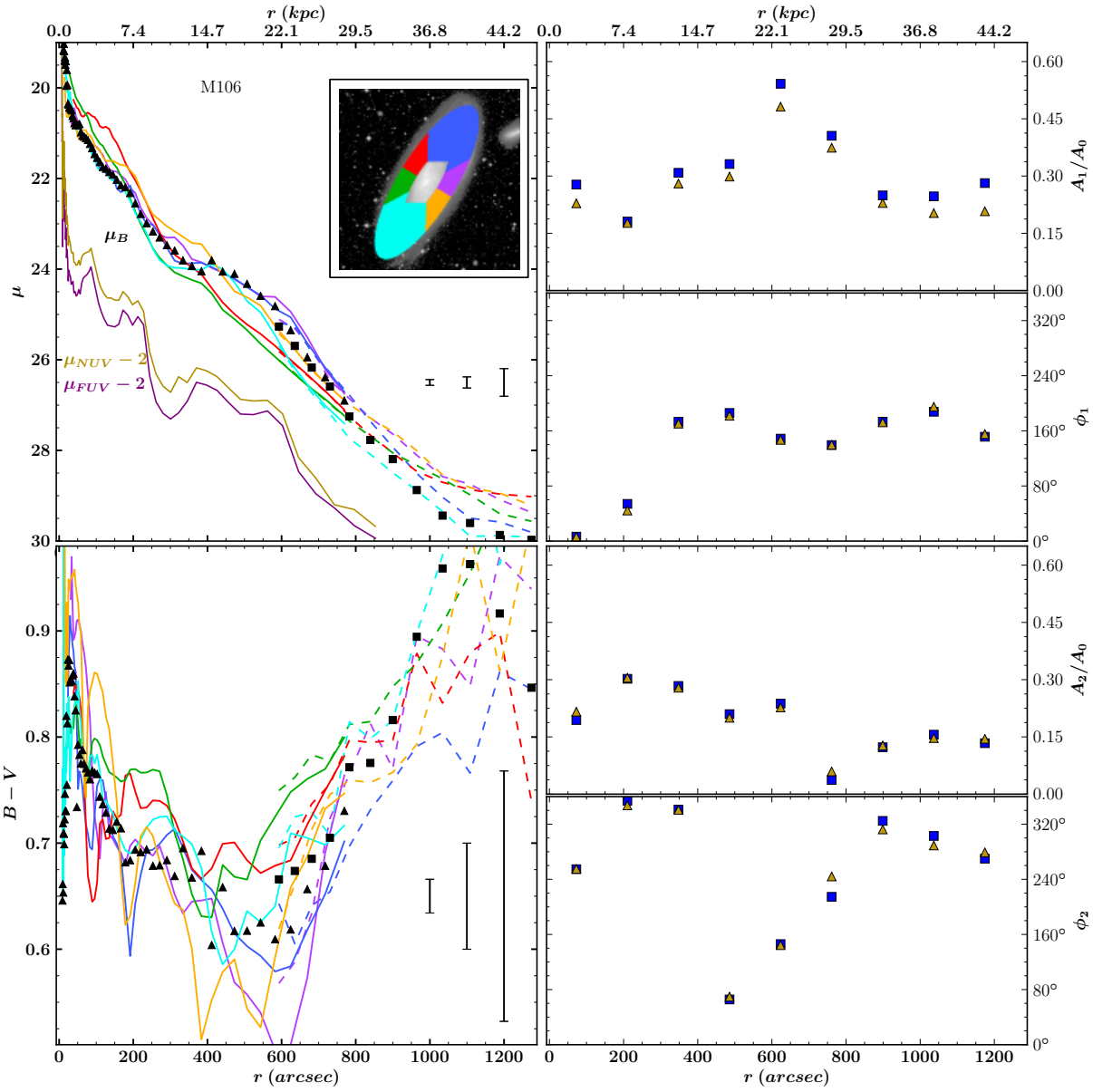

Figure 6. As Figure 2, but of M106. We assume a distance of 7.6 Mpc to M106 (Humphreys et al. 2013), for a disk scale length of 6.0 kpc (based on the inner disk).

arm radius; this peak is due to the southern plume near UGC 7356. Plumes of diffuse starlight and H I are also present on the galaxy's north and south sides along the major axis; the west half of the southernmost plume shows fingers of UV light and blue colors indicating induced star formation, and its proximity to UGC 7356 is suggestive of tidal interaction with that companion (although proximity to tidal features is not an unambiguous indication that a satellite has generated the disturbance; a clear counter-example is the southern tail of M51, generated by the interaction with its companion on the galaxy's north side; Rots et al. 1990; Salo & Laurikainen 2000).

As stated in Section 3.1, M106's classification as either a Type II (downbending) or Type I (unbroken) disk changes depending on the method used to measure its surface brightness profile. This can be seen in the behavior of the angular cuts in Figure 6, in that the eastern side of the galaxy (red and green profiles), where the spiral arms appear weakest, show a profile contiguous with the outer disk, while the spiral arms induce an excess of light over this profile in all of the other angular cuts that appears as a Type II break. This behavior hearkens to the study by Laine et al. (2014), who found that Type II disk breaks tend to follow morphological features such as spiral arms, lenses, or rings. The severity of

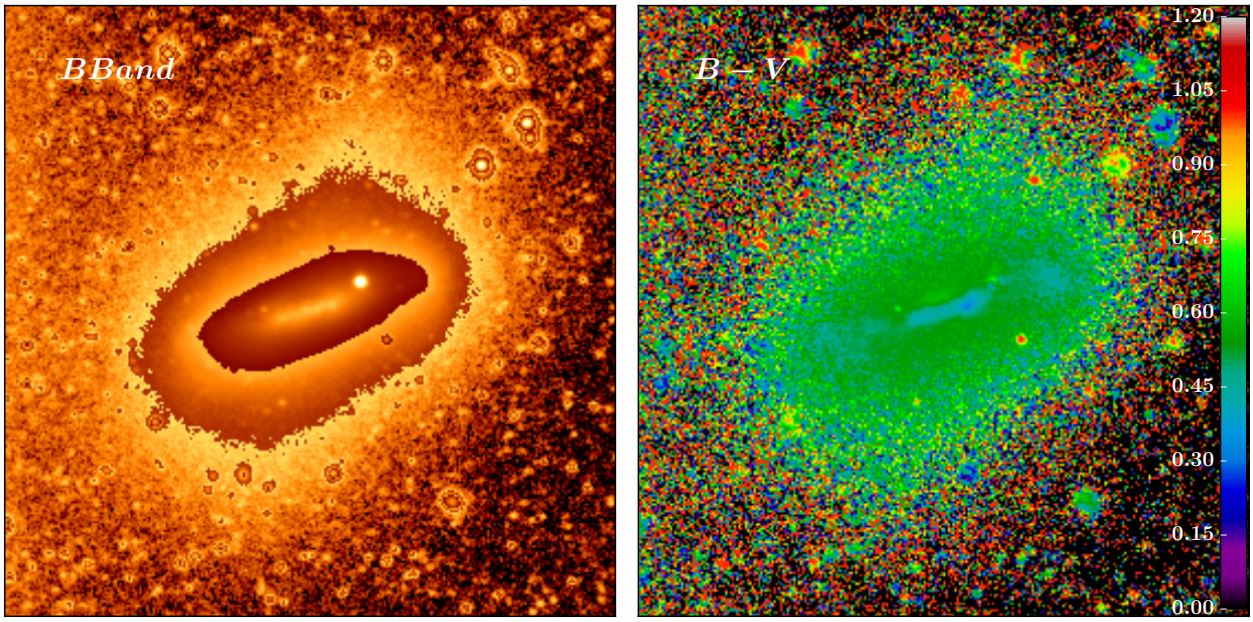

Figure 7. Closeup of NGC 4248. **Left:** *B* band, shown at three levels of brightness (μ_B< 23.5, 23.5 <μ_B< 25.5, and μ_B> 25.5) to highlight the warped inner isophotes, the tidal features on the galaxy's north and south sides, and the very boxy outer isophotes. **Right:** B−V colormap, showing the centrally-concentrated star formation.

the break thus depends on how closely such features are followed in the isophotal analysis; in some cases the choice of isophotes can mask the presence of a disk break entirely or introduce one where none exists. These effects are most obvious in bluer wavelengths due to the presence of high-mass stars in the star-forming regions along spiral arms. In the near-infrared (a fairly robust tracer of stellar mass; Sheth et al. 2010), Laine et al. (2014) note similarity between the inner disk scale lengths of Type I and Type III (antitruncated) disks and the outer disk scale length in Type II disks. Given that M106's profile appears unbroken absent the presence of any spiral arms, one might postulate that the term "break" is a misnomer, and that the inner disks of Type II galaxies are actually elevated in surface brightness over the baseline outer disk due to e.g. recent star formation. This would imply that the differences between Type I and II disks are purely morphological, rather than the product of different formation histories; Type III disks would thus be the true outliers, which is consistent with their comparitive rarity (only ∼20%–30% of disks show Type III breaks; Erwin et al. 2008; Laine et al. 2014).

Examining the very outermost regions of M106's disk, we again see a leveling-off of the azimuthally-averaged surface brightness profile in the last few data points, however as with M94 it appears to be well-modeled simply by a transition into the local background. However, we note that the profiles that follow the galaxy's minor axis (red, green, purple, and yellow) are elevated in surface brightness above the major axis at this extended radius. The patchy diffuse light that can be seen outside of 960″ in Figure 5 likely accounts for this behavior. Given the asymmetry in M106's isophotes, it is unclear if this patchy light is part of M106's outer disk or instead represents an inner halo or thick disk; regardless, we can confidently state that M106's disk extends to at least 1100″ (40 kpc, or ∼6.5 disk scale lengths), making it nearly twice as large in physical size as either M94 or M64.

The tidal features in this galaxy — the southern and northern optical plumes and weak H I tails — are most likely to have originated through tidal interactions with its nearby, bound companions, rather than through a flyby interaction with a more massive companion. A stronger encounter would likely induce more dramatic tidal response, but we see no evidence of elongated tidal tails in M106's vicinity to a limiting surface brightness of μ_B= 29.5. The nearest bright galaxy to M106 is NGC 4144 ($M_B \sim -18$, assuming a distance of 7.5 Mpc; de Vaucouleurs et al. 1991; Seth et al. 2005, but see Jacobs et al. 2009), located some 240 kpc from M106 on the sky (Karachentsev & Kudrya 2014). Given this separation, and NGC 4144's relatively low luminosity, M106's nearby companions certainly have the strongest tidal influence, and NGC 4248's boxy outer isophotes confirm that it is tidally interacting with M106 at some level.

While strong encounters tend to drive centrally concentrated starburst activity (e.g. Barnes & Hernquist 1991; Hernquist & Weil 1992; Hernquist & Mihos 1995; Cox et al. 2008; Hopkins et al. 2009; Powell et al. 2013; Moreno et al. 2015), weaker tidal interactions with satellite galaxies may incite a less-dramatic but longer lived response in the disk outskirts as they orbit the primary over longer timescales. While these low mass interactions may be less efficient at inducing star formation throughout the host (Cox et al. 2008), even a weak starburst in the outer disk may transform the structure and stellar populations of these low surface brightness regions. It may thus be interesting to consider the possibility that NGC 4248 (and to a lesser extent UGC 7356) may be shepherding the gas in M106 in such a way as to produce these outer spiral arms and, at least potentially, trigger star formation in the otherwise low-density outer H I. However, compared to the total extent of the disk, the star formation in M106 is *not* greatly extended; while H I is present at large radius (Wolfinger et al. 2013), only within 20 kpc (∼3 disk scale lengths) is the gas dense enough to form stars. This stands in contrast to the case in the nearby face-on spiral M101, where interactions with its nearby companions have triggered star formation in

the galaxy's diffuse outer disk (Waller et al. 1997; Mihos et al. 2013a). Why, then, was star formation triggered in the outskirts of M101, but seemingly not in M106?

The answer may lie in the fact that in addition to driving tidal resonances in galaxy disks, interactions can also drive non-planar responses including warps and disk heating, which have the potential to shut down star formation. The relative efficacy of these different processes depends not only on the mass ratio of the encounter but also the orbital properties of the encounter. While M101 has a single close satellite (NGC 5477), the galaxy's marked asymmetry and its H I kinematics both argue for a single prograde encounter with the more massive and distant companion galaxy NGC 5474 (Mihos et al. 2012, 2013a). In contrast, M106 has *two* close companions, one of which (NGC 4248) is more massive than M101's close satellite NGC 5477. If the orbital geometry of these satellites is highly non-planar, the two working in concert may tip the dynamical balance towards disk heating rather than tidal compression, suppressing star formation in the outer disk. M106 thus may be an interesting test case concering the influence of fairly massive dwarf satellite galaxies on the star-forming properties of the host, which may be of particular interest in Milky Way studies given the presence of the Magellanic Clouds.

5. DISCUSSION

Despite different local environmental conditions and interaction histories, we see consistent behavior in the photometric properties of these three galaxies' outer disks. In M106 and M94, the onsets of redward gradients in their color profiles correspond to truncations in the UV surface brightness and 21cm emission tracing high column-density H I gas. In M64, the UV emission is constrained to the central disk, and the colors flatten beyond the UV truncation to a similarly red color. The high column-density H I is more extended in this galaxy than in the other two, but is globally at much lower density and hence non-star-forming. What is consistent across all three galaxies is a lack of strong azimuthal color variation in the outer disks, with the interquartile spread in color beyond the break radius always < 0.1 magnitudes (and significantly less in the cases of M94 and M64).

Spiral features also seem to vanish beyond the UV truncation radius. All three galaxies show only mild evidence of azimuthal asymmetry in their outer isophotes, the strongest present in M106, with no evidence of faint extended spiral structure. In these three galaxies, at least, this appears to imply a natural division between the "inner" and "outer" disks; "outer" disks may be defined as the region beyond any evident spiral features and devoid of new star formation, yet still following an exponential surface brightness profile. Here we address the constraints placed by our deep surface photometry on the stellar populations in these outer disks, and compare to studies of outer disk populations in other galaxies. We also consider the role local environment plays in shaping each galaxy's outer disk; in tandem with the inferred stellar populations, these constraints can provide useful clues to the formation and evolutionary histories of outer disks.

5.1. *Outer disk stellar populations*

The similarity in outer disk colors for each galaxies implies a similarity in stellar populations. In all three galaxies, the outer disks display B−Vcolors of approximately 0.75–0.8 at a surface brightness of $\mu_B \sim 27.5$. These colors appear robust against the color uncertainty, which is dominated by fluctuation in the background of the order $\sigma_{B-V} \sim \pm 0.1$ mags at these surface brightnesses (see Section 2.2). These colors also appear independent of the mean background color (as introduced by faint cirrus, unresolved background sources, and residual sky variance); while the background near M64 is fairly red (B−V= 0.85), near both M106 and M94 it is significantly bluer, B−V=0.4-0.5. Indeed, we find similarly red colors in the outskirts of three other disk galaxies we recently studied[4] — M96, M95 (Watkins et al. 2014), and M51 (Watkins et al. 2015) — making this color of B−V= 0.8 a natural anchor-point from which to study the outer disk populations of our galaxies. While broadband colors suffer from the well-known age-metallicity degeneracy (Worthey 1994), these colors can still place some constraints on the outer disk stellar populations. As a fiducial reference, B−V=0.8 is a typical integrated color of an S0a type galaxy (Roberts & Haynes 1994), implying a fairly evolved population.

To explore population constraints in more detail, we model the integrated colors of stellar populations built via a variety of star formation histories and metallicities, constructed using the software SMpy, a Python-based SED modeling code based on the Bruzual & Charlot (2003) population synthesis models (described in: Duncan & Conselice 2015). We constrain these models using the surface brightness and color of the outer disks, as well as the upper limits on their inferred star formation rates (SFRs). At the radius where the disk colors reach B−V=0.8, we do not detect significant FUV flux in any of the galaxies; in M106 and M94 this places a limit on the SFR of ($\lesssim$3-5$\times10^{-5} M_\odot$ yr^{-1} kpc^{-2}). While the limit is higher for M64 due to the FUV image's short exposure time ($\sim 10^{-4} M_\odot$ yr^{-1} kpc^{-2}), it is not so high as to significantly alter our conclusions for this galaxy.

Applying these constraints, we run models using both exponentially-declining histories – SFR(t) $\propto e^{-t/\tau}$ – as well as delayed exponential histories – SFR(t) $\propto te^{-t/\tau}$ (Lee et al. 2010; Schaerer et al. 2013). We adopt varying decay rates (τ) and metallicities for a 10 Gyr timespan, assuming a Chabrier (2003) IMF. A constant star formation history is ruled out by the low current SFR; the timespan required to build enough stars to match the total V band luminosity within the μ_B= 27.5 annulus in each galaxy is > 20 Gyr. Between exponential and delayed exponential histories, consistent behavior emerged: for solar metallicity and below, current-day colors become too blue if $\tau \gtrsim 2$ Gyr, signifying a stellar population dominated by old stars. Metallicities below [Fe/H] ~ -0.7 are ruled out, as these populations produce colors which are too blue regardless of the choice of τ.

While these colors suggest old and only moderately metal poor ([Fe/H > -0.7) populations, significant ambiguity remains due to the age-metallicity degeneracy inherent in broad-band colors. How then do these results compare to other studies of the outskirts of nearby disks using resolved stars, which more directly probe the ages and metallicities of stellar populations?

Resolved imaging studies show a variety of stellar populations present in the outskirts of disk galaxies, indicative of diverse star forming histories. For example, the outskirts of

[4] We note, however, that in the outer disk of M101, we find significantly bluer colors (B−V=0.3–0.5; Mihos et al. 2013a), in congruence with the galaxy's classification as an XUV disk (Thilker et al. 2007). This argues that red outer disk colors are not a universal and systematic artefact of our instrumental setup, such as the extended wings of the PSF. See the Appendix for more details.

NGC 300 and NGC 7793 are populated almost entirely by RGB stars (Vlajić et al. 2009, 2011), while a sizable AGB population was found in the outskirts of NGC 2403 and M33 (Davidge 2003; Barker et al. 2007). M83, a galaxy known to have highly extended star formation (Thilker et al. 2005; Bigiel et al. 2010), contains RGB, AGB, and red supergiant (RSG) stars in its outskirts (Davidge 2010).

The inferred metallicities of resolved outer disk populations also show significant variation from galaxy to galaxy. In NGC 300, Vlajić et al. (2009) found evidence for a metallicity gradient in the outer disk, with metallicities spanning the range [Fe/H]= −0.5 to − 1.0. Similarly low metallicities ([Fe/H]∼ −1.0) have been discovered in the resolved outer disk populations of NGC 2403 and M33 (Davidge 2003; Barker et al. 2007), and even lower metallicites are inferred in NGC 7793's outer disk ([Fe/H]∼ −1.5 Vlajić et al. 2011). Such low metallicities, if characteristic of outer disk populations in general, would lead to colors much bluer than we find in M106, M94, and M64, even taking into account age effects.

However, those studies focused on fairly low mass systems, smaller in mass than the three galaxies in this study (estimated from their maximum rotation velocities listed in the HYPERLEDA catalogue; Makarov et al. 2014), though NGC 2403 is very near in mass to M94 and M64. If we assume that outer disk populations follow their host galaxies' behavior on the well-known galaxy mass-metallicity relationship (e.g. Tremonti et al. 2004), these galaxies would have a higher mean metallicity in their outskirts. Indeed, higher metallicities are inferred in the outer disk populations of the bright spirals M31 ([M/H]∼-0.3 – -0.5; Worthey et al. 2005, Gregersen et al. 2015), M81 ([M/H]∼-0.4 – -0.7; Williams et al. 2009), and M83 (metallicities ranging from ∼20% solar to nearly solar; Davidge 2010). At these metallicities, the integrated colors of the disk would be significantly redder, in line with our deep surface photometry presented here. We also note that metal-rich populations in resolved star studies can be systematically missed due to the the faintness of the metal-rich RGB (e.g. Rejkuba et al. 2005; Harris et al. 2007), complicating comparisons between those studies and deep surface photometry. It may thus be of interest to do more studies directly comparing integrated light colors with resolved photometry in order to better constrain the biases inherent in both methods. We discuss one such bias, the galaxy PSF's influence on our measured colors in the outer isophotes, in the Appendix, though we believe it to be small within μ_B<27.5.

The uniformly red colors, azimuthally smooth distribution, and inferred old, moderately (but not extremely) metal-poor stellar populations at large radius in these galaxies thus place constraints on the formation history of their outer disks. Disk building via continual low-level star formation in the outer disk appears ruled out: such a model would lead to much bluer colors than we observe, and the current rate of star formation is too low to build the amount of light we see in the disk outskirts in a Hubble time. Instead, radial migration (Roškar et al. 2008) emerges as the most likely candidate for disk building at large radius, given the red stellar populations in all three galaxy outskirts, as well as the U-shaped color profiles in the two galaxies still actively forming stars in their inner regions. That said, it is unclear just how far out radial migration can drive stellar populations. Radial migration requires the presence of non-axisymmetric structure such as bars or spiral arms (Sellwood & Binney 2002); significant migration into the outer disk would require the same mechanisms (Minchev et al. 2012; Roškar et al. 2012). In these three galaxies, we find stars extending out to 3–4 scalelengths beyond the edge of the spiral arms; if this behavior is common in other galaxies, it may present a challenge for disk migration models as well. While additional spreading of the outer disk may arise from transient, tidally-driven outer spirals, the galaxies studied here live in fairly low density environments and display no such tidal features. We therefore look forward to new dynamical modeling of disk galaxies that will examine these issues in more detail.

5.2. *Environmental influences*

Under the hierarchical accretion paradigm, galaxy disks are built continually over time, from the inside out, as material from the surrounding environment (both baryonic and not) continually bombard the disk. This accretion can grow disks by depositing stars in disk outskirts (Stewart et al. 2009), triggering extended disk star formation (Whitmore & Schweizer 1995; Weilbacher et al. 2000; Smith et al. 2008; Powell et al. 2013), or moving stars outwards through tidal heating or radial migration (Roškar et al. 2008; Koribalski & López-Sánchez 2009; Khoperskov & Bertin 2015). Yet regardless of how outer disks are built, one would expect to see signatures of this process in these very faint, highly extended regions, where dynamical times are long and material is more loosely bound. However, in the three galaxies studied here, evidence for such accretion signatures is lacking. In M94, the most isolated galaxy of the three, we see only mild lopsidedness in its isophotes, and one extremely faint plume at the very outer edge of the disk, implying a much less chaotic formation history. While M64's past interaction history seems to have greatly damaged the gaseous disk, driving H I inwards and shutting off disk-wide star formation, we again see no evidence for discrete tidal streams. Finally, in the case of M106, a large and luminous disk galaxy with two known and many more suspected satellites, the tidal signatures we do observe are rather weak and likely driven by the two luminous satellites. While we see no strong tidal features in any of the galaxies studied here, the similarity in the star forming properties and stellar populations of their outer disks raises the question of what impact, if any, the local environments might play in shaping their outer disks.

On large scales, the environments of the three galaxies are similiarly devoid of massive companions. Within 1 Mpc, M94 has only a handful of neighbors, all significantly lower in luminosity (the most luminous being NGC 4365, with M_V ∼ −18; de Vaucouleurs et al. 1991; Jacobs et al. 2009). M64 may be even more isolated than M94; its brightest neighbor is the dwarf NGC 4789A, with M_V ∼ −14 (de Vaucouleurs et al. 1991; Jacobs et al. 2009). M106 resides in a somewhat richer environment, with several modestly bright companions within 1 Mpc, although none approach M106 in luminosity. M94 and M64 thus might be considered extremely isolated, while M106 resides in a moderately denser but still fairly sparse environment, more similar to the Local Group (though with no massive companion analogous to M31).

On smaller scales, however, the local environments of the galaxies do appear different. Looking for satellite galaxies with ∼100 kpc, a scale comparable to the Milky Way's satellite system, neither M94 nor M64 have luminous satellites, while M106 has the two mentioned previously: NGC 4248 and UGC 7356. We thus find three levels of environmental influence amongst these three galaxies: M94, being very isolated and apparently undisturbed (Figure 1), may be evolving purely secularly; M64, while also very isolated, likely suf-

fered a recent merger that greatly affected its own morphology and star forming properties (Section 4.2); and M106, living in a denser environment, is presumably being influenced most by its dwarf companions.

Despite their different local environment, M94 and M106 both have similar outer disk structure: a set of extended, star-forming outer spiral arms, beyond which the disk is smoothly distributed and contains an old stellar population. If M94's outer spiral arms are formed secularly, and if M106's outer spiral arms are formed via weak interactions, this implies two very different paths toward a qualitatively similar result. We see no sign of a strongly perturbed outer disk in M106, despite the presence of its satellites. This contrasts with the case of M81, which is similar in luminosity and SFR to M106 (Kennicutt 1998), but where its two more massive companions M82 and NGC 3077 have disrupted its disk outskirts (van der Hulst 1979; Yun et al. 1994; Okamoto et al. 2015). The effect of the satellites on M106's disk appears much gentler — the galaxy may lie in something of a sweet spot, with companions massive enough drive spiral structure (Weinberg 1995; Oh et al. 2008; Choi et al. 2015) and mediate radial migration to build the outer disk, but not massive enough to significantly disrupt it once formed.

The situation for M64 is somewhat more muddled. At first glance, the presence of a Type III upbending break in a post-merger galaxy is consistent with the idea that Type III breaks are driven by strong interactions (Laine et al. 2014) or accretion events (Younger et al. 2007). However, as argued in Section 4.2, the properties of M64's outer component are a poor match for either the induced star formation model or the angular momentum transfer model (Younger et al. 2007). Instead, the changing photometric profile is better explained as a disk-halo transition. That said, the halo is relatively bright: with $\mu_B\sim$ 27 at 10 kpc, it is significantly higher in surface brightness than that of the Milky Way or M31 (Morrison 1993; Gilbert et al. 2012).

If this outer profile is indeed a simply a stellar halo, then in M64 we are seeing a smooth and largely unbroken Type I exponential disk extending all the way out to where it becomes lost in the halo light, at 6 disk scale lengths. The disk is red and azimuthally smooth, save for the very inner regions where some residual star formation continues. With star formation otherwise quenched in the galaxy, M64 may be in the process of becoming an S0 galaxy. Its surface brightness profile is in fact remakably similar to that of ESO 383-45, an S0 galaxy also suspected of having suffered a recent merger (Kemp et al. 2005). S0 galaxies show antitrunctions more frequently than other disk types (Borlaff et al. 2014; Maltby et al. 2015); if mergers drive evolutionary transition from spirals to S0, they may also lead to "spheroidal" antitruncations (denoted Type III-s breaks in Pohlen & Trujillo 2006) by growing the galaxy's halo component.

In these cases, however, the halo-like component forming the antitruncations would by necessity be a different kind of halo than that surrounding the Milky Way, which appears to have been built up over time via satellite disruption rather than from heating of the stellar disk (e.g. Morrison et al. 2000; Bullock & Johnston 2005; Cooper et al. 2010; Ma 2015). Stellar populations in the spheroid beyond the profile breaks would also appear very similar to those in the disk (where they originated), which would explain the relatively flat color profiles such anti-truncated galaxies (including M64) typically exhibit (Zheng et al. 2015). Also, if the halo-like component arose due to heating of the thin disk, and no new thin disk formed from an existing gaseous disk, the antitrunction would also appear in the mass profile of the galaxy; this in fact seems to be the case for Type III disks generally (Bakos et al. 2008; Zheng et al. 2015). If merger-spawned spheroids are the root cause of these antitruncated profiles, such galaxies also should appear more frequently in dense environments (Laine et al. 2014) either because of the heightened rate of interactions or simply the morphology-density relationship raising the likelihood that galaxies will have significant halo components. However, the fact that M64 is apparently quite isolated serves to demonstrate that a dense local environment is not a necessary condition for their formation — one merger event may be sufficient.

Finally, the fact that the outer disks of these three galaxies consist of predominantly old and well mixed populations may simply reflect their host galaxies' local environment. All three galaxies live in low density regions — even the group environment of M106 is sparse, with no large companion galaxies nearby. Weak interactions with low mass satellites may not be sufficient to trigger widespread star formation in outer disks, hence a denser group environment may be more conducive to triggering outer disk star formation. However, even in denser groups the evidence is mixed: M101, the dominant galaxy of its dynamically active group, shows young blue populations in its outer disk (Mihos et al. 2012, 2013a), but in the Leo group, the spirals M95 and M96 both show red outskirts (Watkins et al. 2015). This ambiguity is present in larger surveys as well; Maltby et al. (2012), for example, found little difference in outer disk structure between field and cluster galaxies, while Erwin et al. (2012) found significant differences between field and cluster S0 galaxies (including a complete lack of disk truncations in cluster S0s). Roediger et al. (2012) found that cluster disk galaxies are distributed equally amongst the three disk break types, a significant difference compared to field galaxies (Pohlen & Trujillo 2006), with significant U-shaped age gradients present in all three types, in apparent contradiction to the photometric results of Bakos et al. (2008). Some conflict thus appears to be present regarding environmental influence on outer disk evolution, which may be partially resolved if the immediate, local environment is in fact the driving influence, rather than the global environment.

6. SUMMARY

We have performed deep surface photometry (μ_B=28 - 30) of the nearby galaxies M94, M64, and M106, and incorporated archival UV and 21cm H I data to probe the formation histories of the galaxies' outer disks. All three galaxies exhibit red outer disks beyond a radius corresponding to a truncation in star forming activity and high column-density H I gas in the disk. A Fourier analysis of the azimuthal surface brightness and color profiles of each galaxy's outer disk shows these components are smooth and well-mixed, devoid of spiral arms or significant non-axisymmetric structure.

New star formation in M94 is truncated at $\sim$ 10kpc, beyond which the disk appears azimuthally smooth and red but for some mild lopsidedness. The stellar disk, which seems to be continuous despite the offset inner and outer isophotes, extends to at least ~20kpc, or ~9 scale lengths, with no emergence of a stellar halo down to a surface brightness of $\mu_B\sim$30. Given M94's isolation and smooth undisturbed outer disk, our data favors secularly-driven radial migration of disk populations to explain the galaxy's outer structure. This, combined with its relatively close distance (~4 Mpc) makes M94 an ideal test-bed for follow-up studies investigating how secu-

lar evolution processes such as radial migration affect outer disk formation.

M64 shows a stark star formation truncation only a few kpc from the center, with a low H I column density beyond this radius, and a sharp anti-truncation in the stellar surface brightness beginning around 400″ (9kpc). We trace this anti-truncated disk to ∼19kpc, or ∼13 inner disk scale lengths. M64's strongly anti-truncated profile is likely the signature of a transition from the galaxy's disk to its diffuse stellar halo rather than being a true upbending of the disk surface brightness profile. The recent merger event in M64 appears to have disrupted its gas disk and truncated star formation in all but the inner few kiloparsecs, leading to the galaxy's very flat and red color profile. M64 thus appears to be undergoing a transition from a spiral to an S0 galaxy, an interesting example of merger-driven galaxy transformation in an otherwise isolated environment.

Despite elevated levels of star formation, M106 still shows a clear star formation truncation radius associated with the end of its outer spiral arms at ∼600″ (22kpc). Its stellar disk extends roughly twice this distance beyond this truncation radius, with signs of interaction with its two brightest companion galaxies. We trace M106's stellar disk to ∼40 kpc, or ∼6.5 scale lengths. Although M106 possesses a more robust satellite system than M64 or M94, its smooth outer disk and fairly weak tidal structure argues that these satellites are not dramatically reshaping the disk — instead, they may have helped drive the outward migration of stars in M106's disk without completely disrupting the disk outskirts. M106 may serve as an interesting comparison to the Mily Way's own satellite-driven evolution, given the similarity in morphology, luminosity, and local environment between the two galaxies.

The red colors of these galaxies' outer disks (B−V∼0.8 in their outermost regions) imply predominantly old stellar populations. For exponentially-declining star formation histories, colors this red cannot be achieved for decay rates longer then τ=2 Gyr; and cannot be achieved for *any* τ if metallicities are below [Fe/H]=-0.7. These properties, along with the smoothness of the outer disks, suggest that these parts of the galaxies are not formed through on-going or sporadic star formation, but rather dynamical processes such as heating or radial migration of stars from the inner disk. The lack of a significant young stellar population in these galaxies' outskirts may reflect the sparseness of their local environment; stronger or repeated encounters may be needed to trigger widespread and sustained star formation in outer disks. Additional studies of the detailed stellar populations in outer disks over a wider range of environment would be informative.

However, while all three of the galaxies studied here do live in low density environments, they also appear to have different interaction histories. In this sense, it is interesting that similarly old and smooth stellar populations exist in the outer disks of each galaxy irrespective of the influence of their local environments and recent interaction history — secular processes that operate in a completely isolated galaxy (M94) produce a very similar looking outer disk population as those in a galaxy interacting with companions (M106) or recovering from a recent merger (M64). Furthermore, the large physical extent of these azimuthally smooth outer disks implies a very high efficiency with which stars can be transported via radial migration; whether such extended disks can be built this way remains unclear.

Finally, while red outer disk colors and U-shaped color profiles are frequently cited as evidence of radial migration process (Bakos et al. 2008; Martín-Navarro et al. 2014; Zheng et al. 2015), broadband colors leave a great deal of ambiguity regarding the actual stellar populations producing them. Ambiguity is present even in many resolved population studies; without a halo field to compare to, for example, halo star contamination fractions in outer disk studies remain unconstrained. Measuring stellar kinematics in these extended regions would be ideal to break the disk/halo ambiguity, however this remains infeasible for galaxies beyond ∼1 Mpc. Until such studies are possible, combining data from low-resolution, deep surface photometry (to derive the morphology and integrated properties of extended regions in galaxies) with resolved star studies (to deconstruct the detailed stellar populations and star formation histories of these regions) seems the best option for future studies of outer disks.

7. ACKNOWLEDGEMENTS

This work has been supported by a Jason J. Nassau Graduate Fellowship to AEW, and by the National Science Foundation through award 1108964 to JCM. This work made use of Numpy, SciPy (Oliphant 2007), and MatPlotlib (Hunter 2007). This work made use of THINGS, 'The HI Nearby Galaxy Survey' (Walter et al. 2008). Figures 1, 3, 5, and 7 made use of Min-Su Shin's publicly available code img_scale.py[5]. We would also like to thank Ken Duncan for the use of his code SMpy.

Facility: CWRU:Schmidt - The Burrell Schmidt of the Warner and Swasey Observatory, Case Western Reserve University

APPENDIX

ON THE BURRELL-SCHMIDT PSF

As studies such as this one begin to breach lower and lower surface brightness limits, concerns about instrumental artifacts become much more important. Specifically, these concerns focus on the influence of scattered light, in the form of internal reflections and the extended wings of the point spread function (PSF), which can skew radial surface brightness and color profiles at low surface brightness (for a recent discussion of this problem, see Sandin 2014, 2015). While aggressive anti-reflection coatings on both the filters and dewar windows of the Burrell Schmidt minimize bright reflections in our data, the effect of the extended PSF still remains at a low level, which we explore in more detail here. Before embarking on quantitative tests of the influence of the PSF on the derived photometric profiles, we first note that we have seen no evidence of systematic reddening of galaxy profiles in previous studies using the Burrell Schmidt. While the three galaxies studied here show red outer disks, Schmidt imaging of the spiral galaxy M101 (Mihos et al. 2013a) revealed blue outer isophotes, while deep imaging of the Virgo Cluster showed blueward gradients in the diffuse outer halos of the massive ellipticals M87 (Rudick et al. 2010) and M49 (Mihos et al. 2013b). Redward gradients therefore do *not* seem to be a systematic result of our imaging techniques. However, to assess this

[5] http://dept.astro.lsa.umich.edu/~msshin/science/code/Python_fits_image/

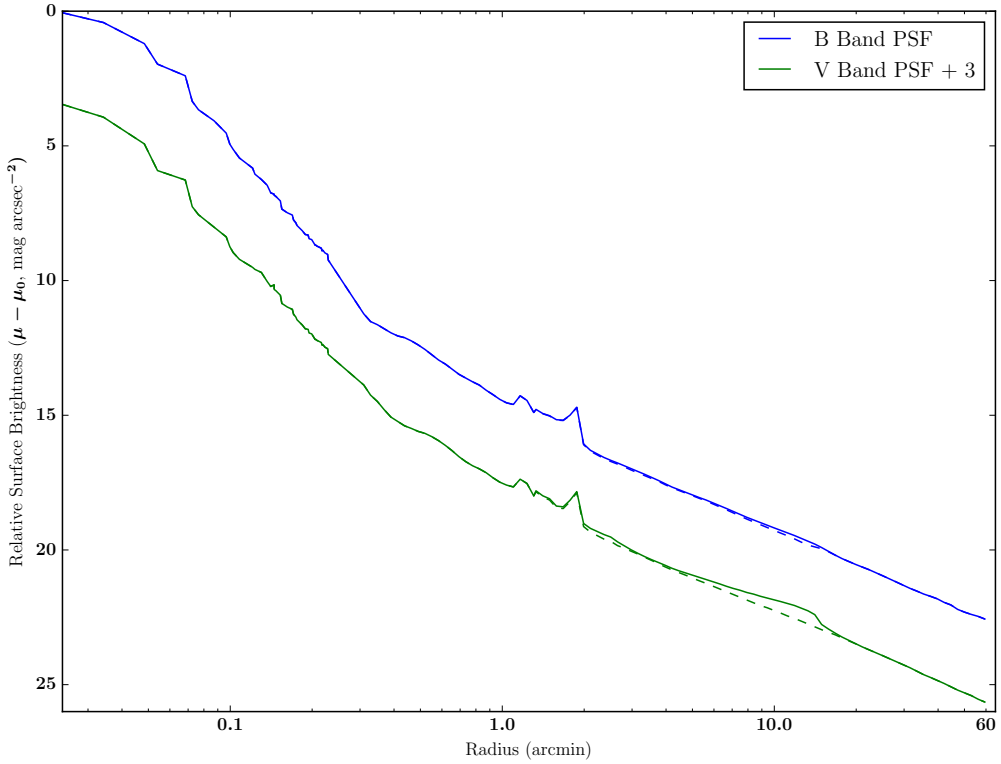

Figure 8. The *B* Band and *V* Band (offset by 3 magnitudes for clarity) radial profiles of the Burrell Schmidt PSF. Solid lines show the profiles including reflections, as measured from our bright star exposures, while dashed lines show the underlying profile wings (with reflections subtracted out). Profiles are normalized such that $\mu_0 = 0$.

effect more quantitatively, in this Appendix we convolve an updated and more accurate measurement of the Burrell Schmidt PSF with a variety of galaxy profiles to quantify its effect on the extracted surface brightness and color profiles of our galaxies.

As discussed briefly in Section 2.1, we measured the Burrell Schmidt PSF using long exposures of bright stars in order to subtract bright reflection halos and the extended PSF wings around bright stars. We show the Burrell Schmidt PSF radial profile in the *B* and *V* bands in Figure 8 out to one degree. An earlier measurement of the *V* band PSF radial profile was published in (Slater et al. 2009, hereafter S09) and (Janowiecki et al. 2010); in the outer wings, this more recent measurement compares well to the older profile, despite being taken several years later and using a different CCD. We note, however, that the inner core profile shown in Figure 8 does differ significantly from that of S09. That earlier study focused on proper subtraction of the outer wings of the PSF, which is insensitive to the shape of the inner core. As such, the core profile of S09 was largely illustrative and not well-determined. In the present study we have worked to produce a much more accurate measurement of the PSF core ($r \lesssim 10''$) by using four stars of different brightnesses to ensure that all pieces of the profile link up correctly. Our updated profile shows that the core profile illustrated in S09 had actually been underestimated significantly. While this difference has little effect on scaled *subtraction* of the outer PSF, it has a dramatic effect on the normalized PSF used for image *convolution*. This is simply due to the fact that there is a range of ∼22 magnitudes in brightness between the core and the PSF wings at $r \sim 1°$, hence most of the flux is contained within the core. As such, an error in the core profile can create significant variation in the intensity of the wings after normalization.

With a more accurate PSF measurement in hand, we tested its influence on the derived photometric profiles by convolving several model galaxies with our normalized PSFs in both bands, and measuring the resulting surface brightness and color profiles. The model galaxies were constructed to represent idealized versions (smooth exponential disks of constant B−V color, with bulges of a constant redder color) of M106, M64, and M101, in order to test the influence of the galaxies' angular sizes and central surface brightnesses. The M106 and M64 models had similar values of μ_0, but different scale lengths (see Figures 4 and 6), while the M101 model had a much lower value of μ_0 and large angular size (M101 is nearly face-on; see Mihos et al. 2013a).

We found that for the M106 and M64 facsimiles, the PSF induces a color change of ΔB−V∼ +0.1 by a surface brightness of μ_B∼28.0. This change in color occurs beyond where our photometry is noise-limited by 0.5 mags arcsec^{-2}; brighter than this surface brightness, the color change induced by the PSF is much smaller than that seen in the data. For example, between μ_B∼25.5 and 26.5, M106 shows a color change of 0.08 magnitudes, while the convolved model galaxy shows a change of only 0.015 magnitudes. Thus, while some of the redward gradient in these galaxies' outer disks may be attributable to the PSF, it is clear that most of the gradient is attributable to changing stellar populations. It should also be noted that, despite its relatively smaller angular size, we see no evidence that the PSF is inducing the anti-truncation seen in M64's outer disk; a significant

PSF-induced anti-truncation is only seen in the convolved model of M64 beyond μ_B~30. Finally, in the M101 facsimile, we see the same 0.1 magnitude color change setting in, but at a much lower surface brightness of μ_B~30.0. This is simply due to M101's lower *central* surface brightness, which scatters less light to large radius in the PSF. Taken as a whole, the results of these various tests thus show that the scientific results presented in this paper (and in previous papers using data taken with the Burrell Schmidt) are robust to PSF influence; the error budget is dominated by photometric uncertainties quantified in Section 2 and 3.

REFERENCES

Aihara, H., Allende Prieto, C., An, D., et al. 2011, ApJS, 193, article id. 29
Athanassoula, E. 1980, A&A, 88, 184
Azzollini, R., Trujillo, I., & Beckman, J. E. 2008, ApJ, 679, L69
Bakos, J., Trujillo, I., Pohlen, M. 2008, ApJ, 683, L103
Barker, M. K., Sarajedini, A., Geisler, D., Harding, P., & Schommer, R. 2007, AJ, 133, 1125
Barnes, J. E. 1988, ApJ, 331, 699
Barnes, J. E., & Hernquist, L. E. 1991, ApJ, 370, L65
Bell, E. F., & de Jong, R. S. 2001, ApJ, 550, 212
Bianchi, L., Madore, B., Thilker, D., et al. 2003, BAAS, 203, 91.12
Bigiel, F., Leroy, A., Walter, F., Brinks, E., de Blok, W. J. G., Madore, B., & Thornley, M. D. 2008, AJ, 136, 2846
Bigiel, F., Leroy, A., Seibert, M., Walter, F., Blitz, L., Thilker, D., & Madore, B. 2010, ApJ, 720, L31
Bland-Hawthorn, J., Vlajić, M., Freeman, K. C., & Draine, B. T. 2005, ApJ, 629, 239
Borlaff, A., Eliche-Moral, M. C., Rodríguez-Pérez, C., Querejeta, M., Tapia, T., Pérez-González, P. G., Zamorano, J., Gallego, J., & Beckman, J. 2014, A&A, 570, 103
Bosma, A., van der Hulst, J. M., & Sullivan, W. T. 1977, A&A, 57, 373
Bournaud, F., Jog, C. J., & Combes, F. 2005, A&A, 437, 69
Braun, R., Walterbos, R. A. M., & Kennicutt, R. C. 1992, Nature, 360, 442
Bresolin, F., Ryan-Weber, E., Kennicutt, R. C., Goddard, Q. 2009, ApJ, 695, 580
Bruzual, G., & Charlot, S. 2003, MNRAS, 344, 1000
Bullock, J. S., & Johnston, K. V. 2005, ApJ, 635, 931
Bush, S. J., Cox, T. J., Hernquist, L., Thilker, D., & Younger, J. D. 2008, ApJ, 683, L13
Cappellari, M., Bertola, F., Burstein, D., Buson, L. M., Greggio, L., & Renzini, A. 1999, ApJ, 515, L17
Chabrier, G. 2003, PASP, 115, 763
Chiappini, C., Matteucci, F., & Gratton, R. 1997, ApJ, 477, 765
Choi, P. I., Guhathakurta, P., & Johnston, K. V. 2002, AJ, 124, 310
Choi, Y., Dalcanton, J. J., Williams, B. F., Weisz, D. R., Skillman, E. D., Fouesneau, M., & Dolphin, A. E. 2015, ApJ, 810, article id. 9
Cooper, A. P., Cole, S., Frenk, C. S., et al. 2010, MNRAS, 406, 744
Courtès, G., & Cruvellier, P. 1961, Compt. Rend. Acad. Sci. Paris, 253, 218
Cox, T. J., Jonsson, P., Somerville, R. S., Primack, J. R., & Dekel, A. 2008, MNRAS, 384, 386
Davidge, T. J. 2003, AJ, 125, 3046
Davidge, T. J. 2006, ApJ, 641, 822
Davidge, T. J. 2007, ApJ, 664, 820
Davidge, T. J. 2010, ApJ, 718, 1428
Debattista, V. P., Mayer, L., Carollo, C. M., Moore, B., Wadsley, J., & Quinn, T. 2006, ApJ, 645, 209
de Blok, W. J. G., Walter, F., Brinks, E., Trachternach, C., Oh, S.-H., & Kennicutt, R. C. 2008, AJ, 136, 2648
de Vaucouleurs, G., de Vaucouleurs, A., Corwin, H. G. Jr., Buta, R. J., Paturel, G., & Fouqué, P. 1991, Third Reference Catalogue of Bright Galaxies (Springer(New York))
Dobbs, C. L., Theis, C., Pringle, J. E., & Bate, M. R. 2010, MNRAS, 403, 625
D'Onghia, E., Vogelsberger, M., Faucher-Giguere, C.-A., & Hernquist, L. 2010, ApJ, 725, 353
Ducati, J. R., yCat, 2237, 0
Duncan, K., & Conselice, C. J. 2015, MNRAS, 451, 2030
Durrell, P. R., Mihos, J. C., Feldmeier, J. J., Jacoby, G. H., & Ciardullo, R. 2003, ApJ, 582, 170
Erwin, P., Pohlen, M., & Beckman, J. E. 2008, AJ, 135, 20
Erwin, P., Gutiérrez, L., & Beckman, J. E. 2012, ApJ, 744, article id. L11
Edvardsson, B., Andersen, J., Gustafsson, B., Lambert, D. L., Nissen, P. E., & Tomkin, J. 1993, A&A, 275, 101
Feldmeier, J. J., Mihos, J. C., Morrison, H. L., Rodney, S. A., & Harding, P. 2002, ApJ, 575, 587
Foreman-Mackey, D., Hogg, D. W., Lang, D., & Goodman, J. 2013, PASP, 125, 925
Fouqué, P., Gourgoulhon, E., Chamaraux, P., & Paturel, G. 1992, A&AS, 93, 211
Fried, D. L. 1966, J. Opt. Soc. Am., 56, 1372
García-Burillo, S., Combes, F., Hunt, L. K., Boone, F., Baker, A. J., Tacconi, L. J., Eckart, A., Neri, R., Leon, S., Schinnerer, E., & Englmaier, P. 2003, A&A, 407, 485
Geha, M., Guhathakurta, P., Rich, R. M., & Cooper, M. C. 2006, AJ, 131, 332
Geller, M. J., & Huchra, J. P. 1983, ApJS, 52, 61
Gilbert, K. M., Guhathakurta, P., Beaton, R. L., et al. 2012, ApJ, 760, article id. 76
Gil de Paz, A., Madore, B. F., Boissier, S., Swaters, R., Popescu, C. C., Tuffs, R. J., Sheth, K., Kennicutt, R. C., Jr., Bianchi, L., Thilker, D., & Martin, D. C. 2005, ApJ, 627, L29
Gregersen, D., Seth, A. C., Williams, B. F., et al. 2015, AJ, 150, 189
Gu, Q.-S., Liao, X.-H., Huang, J.-H., Qu, Q.-Y., & Su, H.-J. 1996, A&A, 314, 18
Gutiérrez, L., Erwin, P., Aladro, R., & Beckman, J. E. 2011, AJ, 142, article id.145
Harris, W. E., Harris, G. L. H., Layden, A. C., & Wehner, E. M. H. 2007, ApJ, 666, 903
Haywood, M. 2006, MNRAS, 371, 1760
Herrmann, K. A., Ciardullo, R., & Sigurdsson, S. 2009, ApJ, 693, L19
Herrmann, K. A. & Ciardullo, R. 2009, ApJ, 705, 1686
Hernquist, L., & Weil, M. L. 1992, Nature, 358, 734
Hernquist, L., & Mihos, J. C., 1995, 448, 41
Hopkins, P. F., Cox, T. J., Younger, J. D., & Hernquist, L. 2009, ApJ, 691, 1168
Humphreys, E. M. L., Reid, M. J., Moran, J. M., Greenhill, L. J., & Argon, A. L. 2013, ApJ, 775, article id. 13

Hunter, J. D. 2007, *Computing in Science & Engineering*, 9, 90
Jacobs, B. A., Rizzi, L., Tully, R. B., Shaya, E. J., Makarov, D. I., & Makarova, L. 2009, AJ, 138, 332
Janowiecki, S., Mihos, J. C., Harding, P., Feldmeier, J. J., Rudick, C., & Morrison, H. L. 2010, ApJ, 715, 972
Kannan, R., Macciò, A. V., Fontanot, F., Moster, B. P., Karman, W., & Somerville, R. S. 2015, MNRAS, 452, 4347
Karachentsev, I. D., Sharina, M. E., Dolphin, A. E., Grebel, E. K., Geisler, D., Guhathakurta, P., Hodge, P. W., Karachentseva, V. E., Sarajedini, A., & Seitzer, P. 2003, A&A, 398, 467
Karachentsev, I. D. 2005, AJ, 129, 178
Karachentsev, I. D., Makarov, D. I., & Kaisina, E. I. 2013, AJ, 145, article id. 101
Karachentsev, I. D., & Kudrya, Y. N. 2014, AJ, 148, 50
Kemp, S. N., de la Fuente, E., Franco-Baldera, A., & Meaburn, J. 2005, ApJ, 624, 680
Kennicutt, R. C., & Edgar, B. K. 1986
Kennicutt, R. C., 1989, ApJ, 344, 685
Kennicutt, R. C. 1998, ApJ, 498, 541
Khoperskov, S. A., & Bertin, G. 2015, MNRAS, 451, 2889
Kim, E., Kim, M., Hwang, N., Lee, M. G., Chun, M.-Y., & Ann, H. B. 2011, MNRAS, 412, 1881
Koribalski, B. S., & López-Sánchez, Á. R. 2009, MNRAS, 400, 1749
Kormendy, J., & Kennicutt, R. C. 2004, ARA&A, 42, 603
Kormendy, J., & Norman, C. A. 1979, ApJ, 233, 539
Kormendy, J. 1982, in Saas-Fee Advanced Course 12: Morphology and Dynamics of Galaxies, ed. L. Martinet & M. Mayor (Sauverny, Switzerland: Observatoire de Genève), 113
Krumholz, M. R., Dekel, A., McKee, C. E. 2012, ApJ, 745, article id. 69
Laine, J., Laurikainen, E., Salo, H., et al. 2014, MNRAS, 441, 1992
Landolt, A. U. 1992, AJ, 104, 372
Lee, S.-K., Ferguson, H. C., Somerville, R. S., Wiklind, T., & Giavalisco, M. 2010, ApJ, 725, 1644
Lemonias, J. J. et al. 2011, ApJ, 733, article id. 74
Luck, R. E., & Lambert, D. L. 2011, AJ, 142, article id. 136
Lupton, R. H., Gunn, J. E., & Szalay, A. S. 1999, AJ, 118, 1406
Lupton, R. H., in SDSS Data Release 8, Transformations Between SDSS Magnitudes and Other Systems, www.sdss3.org/dr8/algorithms/sdssUBVRITransform.php#Lupton2005
Ma, Z. 2015, PhD Thesis, Case Western Reserve University
Maciel, W. J., & Costa, R. D. D. 2010, *IAU Symp. S265, Chemical Abundances in the Universe: Connecting First Stars to Planets*, ed. K. Cunha, M. Spite, & B. Barbuy (Cambridge: Cambridge Univ. Press), 317
Makarov, D., Prugniel, P., Terekhova, N. Courtois, H., & Vauglin, I. 2014, A&A, 570, id.A13
Maltby, D. T., Gray, M. E., Aragón-Salamanca, A., et al. 2012, MNRAS, 419, 669
Maltby, D. T., Aragón-Salamanca, A., Gray, M. E., Hoyos, C., Wolf, C., Jogee, S., & Böhm, A. 2015, MNRAS, 447, 1506
Martin, D. C., Fanson, J., Schiminovich, D., et al. 2005, ApJ, 619, L1
Martín-Navarro, I., Trujillo, I., Knapen, J. H., Bakos, J., & Fliri, J. 2014, MNRAS, 441, 2809
McClure, R. D. 1969, AJ, 74, 50
Mihos, J. C., Harding, P., Spengler, C. E., Rudick, C. S., & Feldmeier, J. J. 2013, ApJ, 762, 82
Mihos, J. C., Harding, P., Rudick, C. S., & Feldmeier, J. J. 2013, ApJ, 764, L20
Mihos, J. C., Keating, K. M., Holley-Bockelmann, K., Pisano, D. J., & Kassim, N. E. 2012, ApJ, 761, 186
Minchev, I., Famaey, B., Combes, F., Di Matteo, P., Mouhcine, M., & Wozniak, H. 2011, A&A, 527, id.A147
Minchev, I., Famaey, B., Quillen, A. C., Di Matteo, P., Combes, F., Vlajić, M., Erwin, P., & Bland-Hawthorn, J. 2012, A&A, 548, 126
Minchev, I., Chiappini, C., & Martig, M. 2013, A&A, 558, id.A9
Morelli, L., Corsini, E. M., Pizzella, A., Dalla, B. E., Coccato, L., & Méndez-Abreu, J. 2015, MNRAS, 452, 1128
Moreno, J., Torrey, P., Ellison, S. L., Patton, D. R., Bluck, A. F. L., Bansal, G., & Hernquist, L. 2015, MNRAS, 448, 1107
Morrison, H. L. 1993, AJ, 106, 578
Morrison, H. L., Mateo, M., Olszewski, E. W., Harding, P., Dohm-Palmer, R. C., Freeman, K. C., Norris, J. E., & Morita, M. 2000, AJ, 119, 2254
Mulder, P. S. & van Driel, W. 1993, A&A, 272, 63
Naab, T., & Ostriker, J. P. 2006, MNRAS, 366, 899
Nassau, J. J. 1945, ApJ, 101, 275
Oh, S. H., Kim, W.-T., Lee, H. M., & Kim, J. 2008, ApJ, 683, 94
Okamoto, S., Arimoto, N., Ferguson, A. M. N., Bernard, E. J., Irwin, M. J., Yamada, Y., & Utsumi, Y. 2015, ApJ, 809, article id. L1
Okamura, S. 1978, PASJ, 30, 91
Oliphant, T. E. 2007, *Computing in Science & Engineering*, 9, 10
Pietsch, W., Vogler, A., Kahabka, P., Jain, A., & Klein, U. 1994, A&A, 284, 386
Pohlen, M., & Trujillo, I. 2006, A&A, 454, 759
Powell, L. C., Bournaud, F., Chapon, D., & Teyssier, R. 2013, MNRAS, 434, 1028
Quach, D., Dyda, S., & Lovelace, R. V. E. 2015, MNRAS, 446, 622
Quinn, P. J., Hernquist, L., & Fullagar, D. P. 1993, ApJ, 403, 74
Radburn-Smith, D. J., Roškar, R., Debattista, V. P., et al. 2011, ApJ, 753, article id. 138
Radburn-Smith, D. J., de Jong, R. S., Seth, A. C., et al. 2011, ApJS, 195, article id. 18
Rejkuba, M., Greggio, L., Harris, W. E., Harris, G. L. H., & Peng, E. W. 2005, ApJ, 631, 262
Rix, H.-W. R., Kennicutt, R. C., Braun, R., & Walterbos, R. A. M. 1995, ApJ, 438, 155
Roberts, M. S., & Haynes, M. P. 1994, ARA&A, 32, 115
Roediger, J. C., Courteau, S., Sánchez-Blázquez, P., & McDonald, M. 2012, ApJ, 758, article id. 41
Roškar, R., Debattista, V. P., Stinson, G. S., Quinn, T. R., Kaufmann, T. & Wadsley, J. 2008, ApJ, 675, L65
Roškar, R., Debattista, V. P., Quinn, T. R., & Wadsley, J. 2012, MNRAS, 426, 2089
Rots, A H., Bosma, A., van der Hulst, J. M., Athanassoula, E., & Crane, P. C. 1990, AJ, 100, 387
Rubin, V. C. 1994, AJ, 107, 173
Rudick, C. S., Mihos, J. C., Harding, P., Feldmeier, J. J., Janowiecki, S., & Morrison, H. L. 2010, ApJ, 720, 569
Salo, H., & Laurikainen, E. 2000, MNRAS, 319, 377
Sánchez, S. F., Rosales-Ortega, F. F., Iglesias-Páramo, J., et al. 2014, A&A, 563, id.A49
Sánchez-Blázquez, P., Courty, S., Gibson, B. K., & Brook, C. B. 2009, MNRAS, 398, 591
Sandin, C. 2014, A&A, 567, 97
Sandin, C. 2015, A&A, 577, 106

Schaerer, D., de Barros, S., & Sklias, P. 2013, A&A, 549, id.A4
Schlafly, E. F., & Finkbeiner, D. P. 2011, ApJ, 737, article id. 103
Schlegel, D. J., Finkbeiner, D. P., & Davis, M. 1998, ApJ, 500, 525
Schönrich, R., & Binney, J. 2009, MNRAS, 399, 1145
Schmidt, M. 1959, ApJ, 129, 243
Schweizer, F. 1976, ApJS, 31, 313
Searle, L., & Zinn, R. 1978, ApJ, 225, 357
Sellwood, J. A., & Binney, J. J. 2002, MNRAS, 336, 785
Seth, A. C., Dalcanton, J. J., & de Jong, R. S. 2005, AJ, 129, 1331
Sheth, K., Regan, M., Hinz, J. L, et al. 2010, PASP, 122, 1397
Slater, C. T., Harding, P., & Mihos, J. C. 2009, PASP, 121, 1267
Smith, B. J., Struck, C., Hancock, M., Giroux, M. L., Appleton, P. N., Charmandaris, V., Reach, W., Hurlock, S., & Hwang, J.-S. 2008, AJ, 135, 2406
Spencer, M., Loebman, S., & Yoachim, P. 2014, AJ, 788, article id. 146
Springel, V., White, S. D. M., Jenkins, A., et al. 2005, Nature, 435, 629
Stewart, K. R., Bullock, J. S., Wechsler, R. H., Maller, A. H., & Zentner, A. R. 2008, ApJ, 683, 597
Stewart, K. R., Bullock, J. S., Wechsler, R. H., & Maller, A. H. 2009, ApJ, 702, 307
Tacconi, L. J., & Young, J. S. 1990, ApJ, 352, 595
Thilker, D. A. Bianchi, L., Boissier, S., et al. 2005, ApJ, 619, L79
Thilker, D. A., Bianchi, L., Meurer, G., et al. 2007, ApJS, 173, 538
Tiede, G. P., Sarajedini, A., & Barker, M. K. 2004, AJ, 128, 224
Toomre, A. 1969, ApJ, 158, 899
Toomre, A., & Toomre, J. 1972, ApJ, 178, 623
Toth, G., & Ostriker, J. P. 1992, ApJ, 389, 5
Tremonti, C. A., Heckman, T. A., Kauffmann, G., et al. 2004, ApJ, 613, 898
Trujillo, I., Martinez-Valpuesta, I., Martínez-Delgado, D., Peñarrubia, J., Gabany, R. J., & Pohlen, M. 2009, ApJ, 704, 618
Tully, B. R., Rizzi, L., Shaya, E. J., Courtois, H. M., Makarov, D. I., & Jacobs, B. A. 2009, AJ, 138, 323
Twarog, B. A. 1980, ApJ, 242, 242
Twarog, B. A., Ashman, K. M., Anthony-Twarog, B. J. 1997, AJ, 114, 2556
van Albada, G. D. 1977, A&A, 61, 297
van der Hulst, J. M. 1979, A&A, 75, 97
van der Hulst, J. M., van Albada, T. S., & Sancisi, R. 2001, *ASP Conf. Ser. 240, Gas and Galaxy Evolution*, ed. J.E. Hibbard, M. Rupen, & J.H. van Gorkum (San Francisco, CA: ASP), 451
van der Kruit, P. C., Oort, J. H., & Mathewson, D. S. 1972, A&A, 21, 169
van der Kruit, P. C. 1979, A&AS, 38, 15
van Eymeren, J., Jütte, E., Jog, C. J., Stein, Y., & Dettmar, R.-J. 2011, A&A, 530, id.A29
Vlajić, M., Bland-Hawthorn, J., & Freeman, K. C., 2009, ApJ, 697, 361
Vlaijć, M., Bland-Hawthorn, J., & Freeman, K. C. 2011, ApJ, 732, article id. 7
Vogelsberger, M., Genel, S., Springel, V., et al. 2014, MNRAS, 444, 1518
Walker, I. R., Mihos, J. C., & Hernquist, L. 1996, ApJ, 460, 121
Waller, W. H., Bohlin, R. C., Cornett, R. H., et al. 1997, ApJ, 481, 169
Walter, F., Brinks, E., de Blok, W. J. G., Bigiel, F., Kennicutt, R. C., Thornley, M. D., & Leroy, A. 2008, AJ, 136, 2563
Walterbos, R. A. M., Braun, R., & Kennicutt, R. C. 1994, AJ, 107, 184
Watkins, A. E., Mihos, J. C., Harding, P., & Feldmeier, J. J. 2014, ApJ, 791, article id. 38
Watkins, A. E., Mihos, J. C., & Harding, P. 2015, ApJ, 800, article id. L3
Weilbacher, P. M., Duc, P.-A., Fritze von Alvensleben, U., Martin, P., & Fricke, K. J. 2000, A&A, 358, 819
Weinberg, M. D. 1995, ApJ, 455, L31
White, S. D. M., & Frenk, C. S. 1991, ApJ, 379, 52
Whitmore, B. C., & Schweizer, F. 1995, AJ, 109, 960
Williams, B. F., Dalcanton, J., Seth, A. C., et al. 2009, AJ, 137, 419
Wolfinger, K., Kilborn, V. A., Koribalski, B. S., Minchin, R. F., Boyce, P. J., Disney, M. J., Lang, R. H., & Jordan, C. A. 2013, MNRAS, 428, 1790
Worthey, G. 1994, ApJS, 95, 107
Worthey, G., España, A., MacArthur, L. A., & Courteau, S. 2005, 631, 820
Wyse, R. F. G., & Gilmore, G. 1992, AJ, 104, 144
Yıldız, M. K., Serra, P., Oosterloo, T. A., Peletier, R. F., Morganti, R., Duc, P.-A., Cuillandre, J.-C., & Karabal, E. 2015, MNRAS, 451, 103
Yong, D., Carney, B. W., Teixera de Almeida, M. L. 2005, AJ, 130, 597
York, D. G., Adelman, J., Anderson, J. E., et al. 2000, AJ, 120, 1579
Younger, J. D., Cox, T. J., Seth, A. C., & Hernquist, L. 2007, ApJ, 670, 269
Yuan, C., & Grosbol, P. 1981, ApJ, 243, 432
Yuan, H. B., Liu, X. W., & Xiang, M. S. 2013, MNRAS, 430, 2188
Yun, M. S., Ho, P. T. P., & Lo, K. Y. 1994, Nature, 372, 530
Zaritsky, D., & Rix, H.-W. 1997, ApJ, 477, 118
Zaritsky, D., & Christlein, D. 2007, AJ, 134, 135
Zaritsky, D., Salo, H., Laurikainen, E., et al. 2013, ApJ, 772, article id. 135
Zheng, Z., Thilker, D. A., Heckman, T. M., et al. 2015, ApJ, 800, article id. 120